



A FOUR-FLUID MHD MODEL OF THE SOLAR WIND/INTERSTELLAR MEDIUM INTERACTION WITH TURBULENCE TRANSPORT AND PICKUP PROTONS AS SEPARATE FLUID

ARCADI V. USMANOV^{1,3}, MELVYN L. GOLDSTEIN², AND WILLIAM H. MATTHAEUS¹

¹ Department of Physics and Astronomy, University of Delaware, Newark, DE 19716, USA; arcadi.usmanov@nasa.gov

² Code 672, NASA Goddard Space Flight Center, Greenbelt, MD 20771, USA

Received 2015 November 6; accepted 2016 February 3; published 2016 March 10

ABSTRACT

We have developed a four-fluid, three-dimensional magnetohydrodynamic model of the solar wind interaction with the local interstellar medium. The unique features of the model are: (a) a three-fluid description for the charged components of the solar wind and interstellar plasmas (thermal protons, electrons, and pickup protons), (b) the built-in turbulence transport equations based on Reynolds decomposition and coupled with the mean-flow Reynolds-averaged equations, and (c) a solar corona/solar wind model that supplies inner boundary conditions at 40 au by computing solar wind and magnetic field parameters outward from the coronal base. The three charged species are described by separate energy equations and are assumed to move with the same velocity. The fourth fluid in the model is the interstellar hydrogen which is treated by separate continuity, momentum, and energy equations and is coupled with the charged components through photoionization and charge exchange. We evaluate the effects of turbulence transport and pickup protons on the global heliospheric structure and compute the distribution of plasma, magnetic field, and turbulence parameters throughout the heliosphere for representative solar minimum and maximum conditions. We compare our results with *Voyager 1* observations in the outer heliosheath and show that the relative amplitude of magnetic fluctuations just outside the heliopause is in close agreement with the value inferred from *Voyager 1* measurements by Burlaga et al. The simulated profiles of magnetic field parameters in the outer heliosheath are in qualitative agreement with the *Voyager 1* observations and with the analytical model of magnetic field draping around the heliopause of Isenberg et al.

Key words: ISM: magnetic fields – magnetohydrodynamics (MHD) – methods: numerical – solar wind – Sun: heliosphere – turbulence

1. INTRODUCTION

The heliosphere is the cavity in the interstellar medium that forms as a result of the interaction between the partially ionized interstellar plasma and the plasma of solar corona that expands away from the Sun to become the supersonic and super-Alfvénic solar wind beyond the heliocentric distance of several solar radii. The solar wind plasma with the embedded magnetic fields fills the heliosphere up to the heliopause, which separates the solar wind from the interstellar plasma. In the outer heliosphere, the solar wind slows down abruptly to subsonic speeds at the termination shock. Unlike the interstellar plasma, interstellar neutral components (mainly, hydrogen and helium) enter the heliosphere freely due to the motion of the Sun relative to the local interstellar medium.

The interaction of the solar wind with the interstellar medium is usually modeled using elaborate multi-fluid or kinetic descriptions for interstellar neutral components. Meanwhile all the existing three-dimensional global heliospheric models (that include the heliospheric interface region) treat the plasmas of solar wind and interstellar medium using the simplistic single-fluid description (e.g., Washimi & Tanaka 1996; Pauls & Zank 1997; Linde 1998; Pogorelov & Matsuda 1998; Ratkiewicz et al. 1998; Ratkiewicz & Ben-Jaffel 2002; Opher et al. 2003, 2009; Borrmann & Fichtner 2005; Izmodenov et al. 2005, 2009, 2014; Pogorelov et al. 2006, 2013). Although the single-fluid description is a reasonable approximation for interstellar plasma with all its constituents being roughly in thermal equilibrium, persistent differences between observed

proton and electron temperatures in the solar wind (e.g., Hundhausen 1972; Cranmer et al. 2009) make the single-fluid approximation hardly applicable to the solar wind plasma. The single-fluid approach is especially inappropriate for the distant solar wind (beyond ~ 10 au), where the interstellar hydrogen density exceeds the solar wind density and effects of interstellar hydrogen become dramatically important. The interaction of solar wind protons with interstellar hydrogen atoms and ionization of the hydrogen by solar radiation give birth to a population of so-called pickup protons, which are thermodynamically different from thermal protons (Fisk & Goldstein 1976; Vasyliunas & Siscoe 1976; Isenberg 1986). While the number density of pickup protons is relatively low, their impact on the solar wind, including its heating and gradual deceleration, is significant. The very high effective temperature ($\sim 10^7$ K) of pickup protons makes them the dominant component of the thermal pressure in the distant solar wind (Burlaga et al. 1996).

The most obvious problem with adopting the single-fluid description for solar wind plasma is that it implies an immediate assimilation of the newborn pickup protons with thermal protons of the solar wind. As a result, single-fluid models predict a steep increase of the plasma temperature with radius beyond ~ 10 au, where the pickup protons play a major role. A modest increase in the temperature of solar wind protons is indeed present in *Voyager 2* data beyond ~ 30 au. However, the steep rise predicted by single-fluid models is in obvious contrast with *Voyager 2* observations. Isenberg (1986) was the first to propose a one-dimensional solar wind model with pickup protons treated by a separate energy equation. Following the approach of Isenberg (1986), a number of one-dimensional models have been developed (e.g., Whang

³ Code 673, NASA Goddard Space Flight Center, Greenbelt, Maryland 20771, USA.

et al. 1995, 2003; Whang 1998; Wang & Richardson 2001). Later on, Usmanov & Goldstein (2006) and Detman et al. (2011) developed three-dimensional models, where pickup protons were treated as a separate fluid.

The radial profile of proton temperature computed by Usmanov & Goldstein (2006) reproduced *Voyager* data if only a small fraction ($\sim 1\%$) of pickup proton energy was assumed to be transferred to thermal protons. The models of Usmanov & Goldstein (2006) and Detman et al. (2011) did not include the heliospheric interface region, where the solar wind and interstellar plasmas interact with each other. The influence of pickup protons as a separate population on the interaction of the solar wind with the interstellar medium has been studied in a two-dimensional (axisymmetric) non-magnetic case using a multi-fluid model (without a separate energy equation for pickup protons) by Fahr et al. (2000) and a kinetic description by Malama et al. (2006). The latter study showed that the positions of the termination shock and heliopause differ from those in the analogous single-fluid-plasma model of Baranov & Malama (1993).

It is widely believed that the pickup protons generate turbulence in the distant solar wind because of an instability that is driven by their initially anisotropic velocity distribution (Wu & Davidson 1972; Fisk & Goldstein 1976; Lee & Ip 1987). The turbulence energy thus produced adds to the existing turbulence and is assumed to dissipate at small spatial scales following a turbulent cascade that supplies the energy that is absorbed by solar wind protons and electrons (e.g., Williams et al. 1995; Matthaeus et al. 1999, 2004; Smith et al. 2001, 2006; Isenberg et al. 2003, 2010; Isenberg 2005; Chalov et al. 2006; Breech et al. 2008, 2009; Gamayunov et al. 2012).

Usmanov et al. (2009, 2011) developed a solar wind model based on numerical solutions of mean-flow Reynolds-averaged magnetohydrodynamic (MHD) equations coupled with a set of turbulence transport equations for turbulence energy, normalized cross-helicity, and correlation scale. A similar approach was taken recently by Wiengarten et al. (2015). The models have been used to study the interaction between the large-scale solar wind and turbulence and to illuminate the role of the turbulence in the temperature distribution of the solar wind. More recently, Usmanov et al. (2012, 2014) extended their model to include interstellar pickup protons as a separate fluid and to study the effects of heating and deceleration of the solar wind. They showed that the computed profiles are in general agreement with *WIND*, *Ulysses* and *Voyager* observations.

Having their focus on the heliospheric interface region, the existing models of the outer heliosphere typically employ simplified patterns for the solar wind and interplanetary magnetic field parameters at their inner boundaries, which are usually placed between 10 and 50 au. The most frequent assumption is that the solar wind is spherically symmetric (e.g., Washimi & Tanaka 1996; Pogorelov & Matsuda 1998; Ratkiewicz et al. 1998; Ratkiewicz & Ben-Jaffel 2002; Opher et al. 2003, 2009; Izmodenov et al. 2005, 2014; Borrmann & Fichtner 2005; Pogorelov et al. 2006). Latitudinal variations at the inner boundary consistent with *Ulysses* observations of the bimodal solar wind near solar minimum have been included, e.g., by Pauls & Zank (1997), Linde (1998), Pogorelov et al. (2013), Provornikova et al. (2014). Although it may seem straightforward to employ three-dimensional solar corona and solar wind models to assign inner boundary conditions, as far as we are aware the existing global heliospheric models have never implemented solar corona/solar wind computations that

extend all the way from the coronal base and employ observations of photospheric magnetic field as inner boundary conditions. In this study, we present for the first time a simulation of the global system comprising not only the outer heliosphere but also the inner heliosphere and solar corona.

In this paper, we further extend the three-fluid solar wind model of Usmanov et al. (2014) by including the heliospheric interface region. To the best of our knowledge, turbulence effects have been never included in the modeling of the solar wind interaction with the local interstellar medium. Our goal has been to construct such a three-dimensional model taking into account turbulence transport and separate energy equations for thermal protons, electrons, pickup protons, and interstellar hydrogen, and then using this model, to study the formation of the heliospheric interface region, including termination shock, heliopause, and bow shock. Unlike the model of Usmanov et al. (2014), where steady-state solutions have been obtained in the reference frame rotating with the Sun, and the distribution of interstellar hydrogen was pre-defined, we use a simplified single-fluid description with separate mass, momentum, and energy equations to describe evolution of interstellar hydrogen inside and outside the heliosphere (Whang 1996, 2010a). Another improvement of the present formulation is that it uses turbulence transport equations that do not rely on the assumption, obviously inappropriate outside the termination shock, that the Alfvén speed is much smaller than the flow speed. The turbulence transport model we employ does not include the effects of eddy viscosity and turbulent resistivity, which have been recently incorporated by Usmanov et al. (2014). An additional limitation is that the turbulence model is based on the premise that the turbulence is incompressible. However, the turbulence that is observed in the inner heliosheath appears to be compressible (Burlaga et al. 2006; Burlaga & Ness 2009) in the sense that the magnetic fluctuations are mainly parallel to the local mean magnetic field. In Section 2, we describe in detail the governing equations, model assumptions and parameters and discuss the initial and boundary conditions. The simulation results are presented in Section 3. In Section 4 we present our conclusions and discuss future extensions of this work.

2. MODEL FORMULATION

2.1. Equations of the Charged Components

The interstellar and solar wind plasmas are assumed to be composed of three co-moving populations: thermal protons, electrons, and pickup protons (Isenberg 1986). Because we neglect the electron mass in comparison with the proton mass, there are two continuity equations, one for each proton population. Each of the three species is described by a separate energy equation. Following Isenberg (1986) and Usmanov et al. (2012, 2014), the time-dependent mass, momentum, and energy conservation equations can be written in the inertial frame as

$$\frac{\partial N_S}{\partial t} + \nabla \cdot (N_S \mathbf{u}) = -q_{\text{ex}}, \quad (1)$$

$$\begin{aligned} \frac{\partial(\rho \mathbf{u})}{\partial t} + \nabla \cdot \left[\rho \mathbf{u} \mathbf{u} - \frac{1}{4\pi} \mathbf{B} \mathbf{B} + \left(P_S + P_E + P_I + \frac{B^2}{8\pi} \right) \mathbf{I} \right] \\ + \frac{\rho G M_{\odot}}{r^2} \hat{\mathbf{r}} = -q_T m_p (\mathbf{u} - \mathbf{u}_H) + q_{\text{ph}} m_p \mathbf{u}, \end{aligned} \quad (2)$$

$$\frac{\partial \mathbf{B}}{\partial t} = \nabla \times (\mathbf{u} \times \mathbf{B}), \quad (3)$$

$$\begin{aligned} \frac{\partial P_S}{\partial t} + (\mathbf{u} \cdot \nabla) P_S + \gamma P_S \nabla \cdot \mathbf{u} + (\gamma - 1) \frac{P_S - P_E}{\tau_{SE}} \\ = -\frac{q_{\text{ex1}} P_S}{N_S}, \end{aligned} \quad (4)$$

$$\frac{\partial N_I}{\partial t} + \nabla \cdot (N_I \mathbf{u}) = q_{\text{ex1}} + q_{\text{ph}}, \quad (5)$$

$$\begin{aligned} \frac{\partial P_I}{\partial t} + (\mathbf{u} \cdot \nabla) P_I + \frac{5}{3} P_I \nabla \cdot \mathbf{u} = -\frac{q_{\text{ex2}} P_I}{N_I} \\ + q_T \left[\frac{P_H}{N_H} + \frac{m_p (\mathbf{u} - \mathbf{u}_H)^2}{3} \right], \end{aligned} \quad (6)$$

$$\begin{aligned} \frac{\partial P_E}{\partial t} + (\mathbf{u} \cdot \nabla) P_E + \gamma P_E \nabla \cdot \mathbf{u} + (\gamma - 1) \frac{P_E - P_S}{\tau_{SE}} \\ = (\gamma - 1) q_{\text{ph}} \varepsilon_0, \end{aligned} \quad (7)$$

where N_S and N_I are the thermal proton and pickup proton number densities, \mathbf{u} is the mass velocity, \mathbf{B} is the magnetic field, and P_S , P_I and P_E are the thermal proton, pickup proton and electron thermal pressure, respectively. Other notations are: the velocity \mathbf{u}_H and number density N_H of interstellar hydrogen, the mass density $\rho = (N_S + N_I) m_p$, where m_p is the proton mass, the universal gravitational constant G , the solar mass M_\odot , the unit matrix \mathbf{I} , the unit vector in the radial direction \hat{r} , the adiabatic index $\gamma (=5/3)$, and the average energy of photoelectrons $\varepsilon_0 = 30$ eV (Isenberg 1986). The time scale of Coulomb collisions between thermal protons and electrons is $\tau_{SE} = 1/\nu_E$, where ν_E is the electron–proton collision rate (Hartle & Sturrock 1968)

$$\nu_E = \frac{8(2\pi m_e)^{1/2} N_E e^4 \ln \Lambda}{3m_p (k_B T_E)^{3/2}}, \quad (8)$$

and $\ln \Lambda$ is the Coulomb logarithm

$$\ln \Lambda = \ln \left[\frac{3(k_B T_E)^{3/2}}{2\pi^{1/2} e^3 N_E^{1/2}} \right]. \quad (9)$$

Other quantities in Equations (8) and (9) are: the electron mass m_e , the elementary charge e , the number density of electrons $N_E = N_S + N_I$ (from the requirement of charge neutrality), the Boltzmann constant k_B , and the electron temperature $T_E (=P_E/k_B N_E)$.

Following Isenberg (1986), we use the simplified form of source terms suggested by Holzer (1972) that describe the photoionization and charge exchange of protons and interstellar hydrogen. The production rates of pickup protons from interstellar hydrogen by charge exchange with thermal protons, by charge exchange with pickup protons, and by photoionization are written as: $q_{\text{ex1}} = \sigma N_S N_H u^*$, $q_{\text{ex2}} = \sigma N_I N_H u^*$, and $q_{\text{ph}} = \nu_0 (r/r_0)^2 N_H$, respectively, where $u^* = |\mathbf{u} - \mathbf{u}_H|$ is the mean relative velocity of the plasma flow with respect to the interstellar hydrogen, $\nu_0 = 0.9 \times 10^{-7} \text{ s}^{-1}$ is the photoionization rate per hydrogen atom at the heliocentric distance $r_0 = 1$ au, and $\sigma = 2 \times 10^{-15} \text{ cm}^2$ is the mean charge exchange cross section of a hydrogen atom. In this study, we assume that σ is constant (Whang 1998) and that ionization by

electron impact is negligible. The total production rate of pickup protons is $q_T = q_{\text{ex1}} + q_{\text{ex2}} + q_{\text{ph}}$.

2.2. Interstellar Hydrogen Equations

We recognize that in general a multi-fluid (Pauls et al. 1995; Zank et al. 1996) or kinetic (Baranov et al. 1991; Malama 1991; Baranov & Malama 1993; Heerikhuisen et al. 2006) description of interstellar hydrogen may eventually be required, but in this study we employ the one-fluid approach of Whang (1996, 2010a), which accounts only for hydrogen atoms of interstellar origin and neglects hydrogen atoms produced by charge exchange between protons and interstellar hydrogen. In this approach, the mass, momentum, and energy conservation equations for interstellar hydrogen are

$$\frac{\partial N_H}{\partial t} + \nabla \cdot (N_H \mathbf{u}_H) = -q_T, \quad (10)$$

$$\begin{aligned} \frac{\partial (\rho_H \mathbf{u}_H)}{\partial t} + \nabla \cdot (\rho_H \mathbf{u}_H \mathbf{u}_H + P_H \mathbf{I}) \\ = -q_T m_p \mathbf{u}_H - \rho_H (1 - \mu_H) \frac{GM_\odot}{r^2} \hat{r}, \end{aligned} \quad (11)$$

$$\begin{aligned} \frac{\partial (\rho_H E_H)}{\partial t} + \nabla \cdot [\rho_H \mathbf{u}_H (E_H + P_H/\rho_H)] \\ = -q_T m_p E_H - \rho_H (1 - \mu_H) \frac{GM_\odot u_{Hr}}{r^2}, \end{aligned} \quad (12)$$

where N_H , \mathbf{u}_H , and P_H are the number density, mass velocity, and thermal pressure of interstellar hydrogen, respectively; $\rho_H = m_p N_H$ is the hydrogen mass density, $E_H = (u_H^2 + 3P_H)/2\rho_H$ is the total energy per unit mass of interstellar hydrogen, and μ_H is the ratio of the solar radiation pressure force to the gravitational attraction force. Following Whang (1996, 2010a), we assume $\mu_H = 1$, so the last terms in Equations (11) and (12) are assumed to be negligible.

2.3. Reynolds Averaged Mean-flow Equations

We apply the Reynolds decomposition of dependent variables into mean and fluctuating parts to Equations (1)–(7) and assume that the turbulence is locally incompressible, i.e., the fluctuations of densities and thermal pressures can be neglected (Usmanov et al. 2009, 2011, 2012, 2014). Retaining the same notation for dependent variables that represent now ensemble averages we can re-write Equations (2)–(4) and (6)–(7) as

$$\begin{aligned} \frac{\partial (\rho \mathbf{u})}{\partial t} + \nabla \cdot \left[\rho \mathbf{u} \mathbf{u} - \frac{1}{4\pi} \mathbf{B} \mathbf{B} + (P_S + P_E) \right. \\ \left. + P_I + \frac{B^2}{8\pi} + \frac{\langle B^2 \rangle}{8\pi} \right] \mathbf{I} + \mathcal{R} \Big] + \frac{\rho GM_\odot}{r^2} \hat{r} \\ = -q_T m_p (\mathbf{u} - \mathbf{u}_H) + q_{\text{ph}} m_p \mathbf{u}, \end{aligned} \quad (13)$$

$$\frac{\partial \mathbf{B}}{\partial t} = \nabla \times [\mathbf{u} \times \mathbf{B} + (4\pi \rho)^{1/2} \varepsilon_m], \quad (14)$$

$$\begin{aligned} \frac{\partial P_S}{\partial t} + (\mathbf{u} \cdot \nabla) P_S + \gamma P_S \nabla \cdot \mathbf{u} + (\gamma - 1) \frac{P_S - P_E}{\tau_{SE}} \\ = -\frac{q_{\text{ex1}} P_S}{N_S} + f_p Q_1, \end{aligned} \quad (15)$$

$$\frac{\partial P_I}{\partial t} + (\mathbf{u} \cdot \nabla) P_I + \frac{5}{3} P_I \nabla \cdot \mathbf{u} = -\frac{q_{\text{ex}2} P_I}{N_I} + q_T \left[\frac{P_H}{N_H} + \frac{m_p (\mathbf{u} - \mathbf{u}_H)^2}{3} + \frac{m_p \langle u'^2 \rangle}{3} \right] - Q_2, \quad (16)$$

$$\frac{\partial P_E}{\partial t} + (\mathbf{u} \cdot \nabla) P_E + \gamma P_E \nabla \cdot \mathbf{u} + (\gamma - 1) \frac{P_E - P_S}{\tau_{SE}} = (\gamma - 1) q_{\text{ph}} \varepsilon_0 + (1 - f_p) Q_1, \quad (17)$$

where $\langle \dots \rangle$ denotes the Reynolds ensemble averaging operator, \mathbf{u}' and \mathbf{B}' are fluctuating components of the velocity and magnetic field, which obey the conditions $\langle \mathbf{u}' \rangle = 0$ and $\langle \mathbf{B}' \rangle = 0$, $\mathcal{R} = \langle \rho \mathbf{u}' \mathbf{u}' - \mathbf{B}' \mathbf{B}' / 4\pi \rangle$ is the Reynolds stress tensor, and $\varepsilon_m = \langle \mathbf{u}' \times \mathbf{B}' \rangle (4\pi\rho)^{-1/2}$ is the mean turbulent electric field. Note that we do not apply the Reynolds decomposition to the interstellar hydrogen quantities and that Equations (1) and (5) retain their form after applying the Reynolds averaging. The source terms introduced in Equations (15)–(17) are the turbulent heating Q_1 distributed between thermal protons and electrons according to the fraction f_p (see Breech et al. 2009), and the energy loss Q_2 by pickup protons to feed turbulent fluctuations. The form of Q_1 and Q_2 will be defined in the next section.

2.4. Turbulence Transport Equations

The turbulence transport model that we use here is based on the equations derived in Usmanov et al. (2014). However, we do not assume that the flow speed is much larger than the Alfvén speed. Under the condition that the velocity and magnetic field fluctuations are transverse to the mean magnetic field \mathbf{B} , the transport equations for the turbulence quantities from Usmanov et al. (2014) (see Equations (A3), (A4), and (18)) can be written in the inertial reference frame as

$$\begin{aligned} \frac{\partial Z^2}{\partial t} + (\mathbf{u} \cdot \nabla) Z^2 + \frac{Z^2}{2} \nabla \cdot \mathbf{u} + \frac{2}{\rho} \mathcal{R} : \nabla \mathbf{u} - \frac{\sigma_D Z^2}{2} \nabla \cdot \mathbf{u} \\ + 2\varepsilon_m \cdot (\nabla \times \mathbf{V}_A) - (\mathbf{V}_A \cdot \nabla) (Z^2 \sigma_c) + Z^2 \sigma_c \nabla \cdot \mathbf{V}_A \\ + \frac{m_p Z^2}{2\rho} [2q_T (1 + \sigma_D) + q_{\text{ph}} (1 - \sigma_D)] \\ = -\frac{\alpha f^+(\sigma_c) Z^3}{\lambda} + \dot{E}_{PI}, \end{aligned} \quad (18)$$

$$\begin{aligned} \frac{\partial (Z^2 \sigma_c)}{\partial t} + (\mathbf{u} \cdot \nabla) (Z^2 \sigma_c) + \frac{Z^2 \sigma_c}{2} \nabla \cdot \mathbf{u} + \frac{2}{\rho} \mathcal{R} : \nabla \mathbf{V}_A \\ + 2\varepsilon_m \cdot (\nabla \times \mathbf{u}) - (\mathbf{V}_A \cdot \nabla) Z^2 + (1 - \sigma_D) Z^2 \nabla \cdot \mathbf{V}_A \\ + \frac{Z^2 \sigma_c}{2\rho} (2q_T + q_{\text{ph}}) m_p = -\frac{\alpha f^-(\sigma_c) Z^3}{\lambda}, \end{aligned} \quad (19)$$

$$\frac{\partial \lambda}{\partial t} + (\mathbf{u} \cdot \nabla) \lambda = \beta f^+(\sigma_c) Z - \frac{\beta \lambda \dot{E}_{PI}}{\alpha Z^2}. \quad (20)$$

In the above equations, the statistical quantities describing turbulence are: the doubled fluctuation energy per unit mass $Z^2 = \langle u'^2 + b'^2 \rangle$, the normalized cross helicity $\sigma_c = 2 \langle \mathbf{u}' \cdot \mathbf{b}' \rangle Z^{-2}$, and the correlation length λ , where $\mathbf{b}' = \mathbf{B}' (4\pi\rho)^{-1/2}$. Other notations are: the normalized energy difference $\sigma_D = \langle u'^2 - b'^2 \rangle Z^{-2}$, the Alfvén velocity $\mathbf{V}_A = \mathbf{B} (4\pi\rho)^{-1/2}$,

the Kármán–Taylor constants α and β related as $\alpha = 2\beta$ (Breech et al. 2008), and functions of cross helicity $f^\pm(\sigma_c) = (1 - \sigma_c^2)^{1/2} [(1 + \sigma_c)^{1/2} \pm (1 - \sigma_c)^{1/2}] / 2$ (Matthaeus et al. 2004). The energy that is lost by pickup protons and converted into turbulence energy, is approximated as (Williams et al. 1995; Isenberg et al. 2003; Smith et al. 2004, 2006; Breech et al. 2008; Usmanov et al. 2012, 2014)

$$\dot{E}_{PI} = f_D \frac{u^* V_A}{\rho} q_T m_p, \quad (21)$$

where V_A is the Alfvén velocity and f_D is a parameter that accounts for the details of isotropization process of newborn pickup protons. Following Breech et al. (2008), we assume that f_D is a constant.

It is usually observed in *Voyager* data that the magnetic fluctuation energy is about twice the kinetic fluctuation energy (Matthaeus & Goldstein 1982), and this corresponds to $\sigma_D \approx -1/3$. Therefore we treat σ_D as a constant parameter. The first term on the right-hand side of Equation (18) is the loss rate of turbulence energy as a result of its conversion into thermal energy of protons and electrons, and the second term is the turbulent energy generated by pickup protons. The source terms in Equations (15)–(17) can be written then as

$$Q_1 = \frac{(\gamma - 1) \alpha f^+(\sigma_c) \rho Z^3}{2\lambda}, \quad Q_2 = \frac{\rho \dot{E}_{PI}}{3}. \quad (22)$$

In this study, we restrict ourselves with the special case of the turbulence axisymmetric with respect to the mean field \mathbf{B} and with polarizations transverse to that direction (Usmanov et al. 2009, 2011, 2012; Wiengarten et al. 2015). We will not consider the effects of eddy viscosity and turbulent resistivity as was done by Usmanov et al. (2014). Consequently, the Reynolds stress tensor can be reduced to (Usmanov et al. 2009, 2011, 2012)

$$\mathcal{R} = \frac{\sigma_D \rho Z^2}{2} (\mathbf{I} - \hat{\mathbf{B}} \hat{\mathbf{B}}), \quad (23)$$

where $\hat{\mathbf{B}}$ is a unit vector along \mathbf{B} . Usmanov et al. (2014) have shown that the eddy viscosity/turbulent resistivity effects decrease cross helicity and increase turbulence energy, correlation length, and temperatures of solar wind protons and electrons. Although the effects are significant, especially in high-shear regions, we do not anticipate that adding them to our formalism, which we leave for future work, will change notably the results of the present study.

2.5. The Integrated System of Equations

The governing system of equations combines the mean-flow plasma and magnetic field Equations (1), (5), (13)–(17), turbulence transport Equations (18)–(20), and interstellar hydrogen Equations (10)–(12). All the equations transformed to non-dimensional variables are given in a quasi-conservation component form in the Appendix. In the present work, we neglect the terms with the mean turbulent electric field ε_m (so those terms are omitted in Equation (24)), and construct steady-state solutions of (24) by time integration for given initial and boundary conditions until a steady state is achieved.

2.6. Initial and Boundary Conditions

The inner boundary conditions at 40 au are extracted from the solar wind model with eddy viscosity and turbulent resistivity of Usmanov et al. (2014), which in turn uses a three-dimensional

MHD coronal model with WKB Alfvén waves (Usmanov et al. 2000; Usmanov & Goldstein 2003) as input at 0.3 au.

The initial conditions (before the time relaxation starts at $t=0$) are imposed throughout the computational domain as a uniform flow with parameters corresponding to the local interstellar medium. The interstellar medium flow direction is set to the arrival direction of the interstellar helium with the Heliocentric Aries Ecliptic (HAE_{J2000}) longitude and latitude ($255^\circ.4$, $5^\circ.2$) derived by Lallement et al. (2010) from *Solar and Heliospheric Observatory* observations. The heliographic inertial (HGI_{J2000}) coordinates of the helium velocity vector are respectively ($359^\circ.0$, $-5^\circ.1$). The interstellar medium parameters are set as follows: the plasma density is 0.1 cm^{-3} , the mass velocity is 26 km s^{-1} , and the proton and electron temperatures are 6135 K. The distribution of interstellar hydrogen in the initial state is taken to be uniform throughout the entire computational domain with the number density of 0.125 cm^{-3} and the velocity and temperature being the same as that of the interstellar plasma.

The turbulence in the undisturbed interstellar medium is assumed to be vanishingly small with the turbulence parameters arbitrarily chosen as $Z^2 = 10^{-2} \text{ km}^2 \text{ s}^{-2}$, $\sigma_c = 0$, and $\lambda = 1 \text{ au}$. Following Breech et al. (2008, 2009), we set the normalized energy difference $\sigma_D = -1/3$, the isotropization parameter $f_D = 0.25$, and the fraction of turbulent energy absorbed by protons $f_p = 0.6$. The values of the Kármán–Taylor constants are set as $\alpha = 0.128$ and $\beta = 0.064$ (see Usmanov et al. 2014).

The interstellar magnetic field strength is set to $2 \mu\text{G}$ (0.2 nT). Its direction is assumed to be the center of the ribbon of enhanced energetic neutral atom emission discovered by *IBEX* spacecraft (Fuselier et al. 2009; McComas et al. 2009). The ribbon center is widely believed to coincide with the direction of undisturbed interstellar magnetic field (Funsten et al. 2009, 2013; McComas et al. 2013; Grygorczuk et al. 2014). The HAE_{J2000} longitude and latitude of the ribbon center as derived by Funsten et al. (2013) are ($219^\circ.2$, $39^\circ.9$). The corresponding HGI_{J2000} coordinates are ($139^\circ.1$, $35^\circ.4$). This direction differs by $\sim 41^\circ$ from the direction of the draped interstellar magnetic field beyond the heliopause that has been observed by *Voyager 1* (Burlaga & Ness 2014).

The inner boundary parameters are fixed on the initial values except for the interstellar hydrogen for which the boundary is treated as an outflow boundary with zero-order extrapolation from the interior points near the boundary. The upstream (downstream) part of the outer boundary is considered as an inflow (outflow) boundary on which all flow parameters are specified (first-order extrapolation from the grid points adjacent to boundary is used). The assumed interstellar parameters imply that the flow speed (26 km s^{-1}) exceeds the fast magnetosonic speed (19 km s^{-1}). Therefore, a bow shock is expected to develop outside the heliopause to slow down, compress and deflect the interstellar plasma around the heliosphere. Note that due to some uncertainty with the actual values of interstellar medium parameters, the existence of bow shock is in doubt (see, e.g., McComas et al. 2012).

2.7. The Computational Grid and Numerical Method

Computations are performed on a spherical grid in the HGI_{J2000} coordinates. The grid is composed of three overlapping spherical segments (Usmanov 1996; Usmanov et al. 2012) between 40 and 1200 au. We apply a logarithmic transformation of the governing equations to the new radial coordinate $r' = \ln(r/r_0)$, where r_0 is the radius of the inner boundary (Usmanov 1993). Under the

assumption of a constant grid resolution $\Delta r'$ along r' , the grid spacing Δr is a linearly increasing function of r : $\Delta r = r\Delta r'$. Our grid consists of 300 points distributed equidistantly along r' . As a result, the grid spacing in r increases from 0.5 au near the inner boundary to 13.5 au near the outer boundary. The angular grid spacing is universally fixed at $1^\circ.5$. To integrate the coupled system of Equations (24), we apply the Central Weighted Essentially Non-Oscillatory (CWENO) spatially third-order reconstruction algorithm of Kurganov & Levy (2000). The smoothness indicators of the algorithm are chosen to be based on the variations of the thermal proton density. The spatial CWENO discretization is merged with the Strong Stability-Preserving Runge–Kutta first-order time integration scheme of Gottlieb et al. (2001). To maintain the divergence-free condition for the magnetic field, we use the method of Powell (1994), which is based on the idea that any non-zero divergence is transported out of the computational domain. The method requires adding source terms proportional to $\nabla \cdot \mathbf{B}$ to the momentum and induction Equations (13)–(14). Similar terms are added also to Equations (18)–(19) (see the Appendix).

3. SIMULATION RESULTS

Figure 1 shows color maps of a steady-state solution from 40 to 600 au in the meridional plane containing the interstellar upwind direction. The solution is a result of time integration of Equation (24), which continues up to a total physical evolution time of $t = 350$ years, by which time, the solution has achieved a dynamical equilibrium. The inner boundary conditions at 40 au are representative of solar minimum conditions and have been extracted from the axisymmetric solar wind solution for a magnetic dipole on the Sun aligned with the solar rotation axis as shown in Figure 2 of Usmanov et al. (2014). Because the inner boundary conditions are axisymmetric, there are no effects of solar rotation. The three heliospheric boundaries are clearly seen in most of the plots in Figure 1: the termination shock separating the supersonic and super-Alfvénic solar wind from the relatively slow solar wind in the inner heliosheath, the heliopause separating the compressed solar wind from the compressed interstellar plasma, and the bow shock that separates the pristine and compressed interstellar plasma. The solar wind inside the termination shock is slower and denser near the equatorial plane and faster and more tenuous at higher latitudes. The proton density also increases in the heliospheric tail near the equator outside the termination shock. A gradual slowdown of the fast wind with heliocentric distance due to the interaction with interstellar hydrogen with the subsequent energy transfer to pickup protons is easily distinguishable in Figure 1(a). The proton and electron temperatures are lower both near the equator and the pole and are enhanced in mid latitudes. Because of the lower dynamic pressure and magnetic field strength near the helioequator, the heliopause is caving in in the vicinity of the helioequator on the upwind side. The compressed interstellar magnetic field is especially strong in this region. The interstellar plasma deflected around the termination shock is clearly seen in the plot of meridional velocity u_θ (Figure 1(f)) that reaches the values above 200 km s^{-1} . (The change of sign on the pole reflects the definition of the meridional component in spherical coordinates.)

Figure 1(h) shows that the pickup proton density is enhanced in the outer heliosheath and is relatively low inside the termination shock. Meanwhile, the thermal pressure of pickup protons (Figure 1(g)) dominates in the inner heliosheath, especially around the upwind direction. The neutral hydrogen

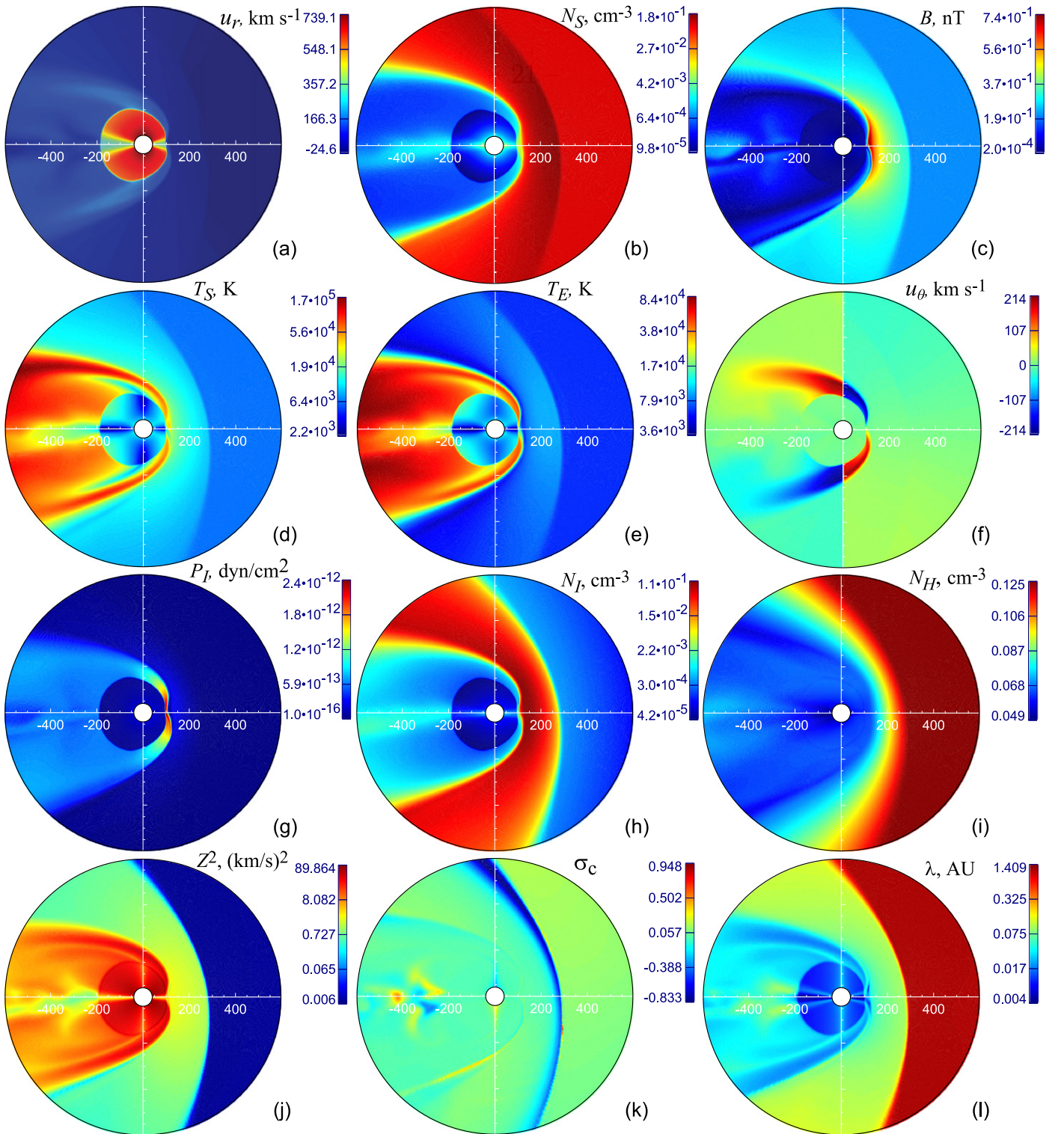


Figure 1. Contour plots of computed parameters in the meridional plane containing the interstellar upwind direction from 40 to 600 au for the 0° -model (an axisymmetric solar wind from a magnetic dipole on the Sun aligned with the solar rotation axis): (a) radial velocity u_r , (b) number density of thermal protons N_S , (c) magnetic field magnitude B , (d) thermal proton temperature T_S , (e) electron temperature T_E , (f) meridional velocity u_θ , (g) pickup proton pressure P_l , (h) pickup proton density N_l , (i) interstellar hydrogen density N_H , (j) turbulence energy per unit mass Z^2 , (k) cross helicity σ_c , and (l) correlation length scale λ .

is one of two variables in Figure 1 that are not sensitive to the termination shock. The second variable is the cross helicity σ_c , the distribution of which outlines the bow shock and heliopause, but is not affected by the termination shock. We have identified the term in Equation (19) responsible for the increased negative σ_c right inside the bow shock as $-(\mathbf{V}_A \cdot \nabla)Z^2$ (6th term in the

left-hand side). The generation of σ_c is therefore the effect of inhomogeneities in Z^2 along the magnetic field. This effect has been discussed by Yokoi et al. (2010) and Yokoi (2011). The “four-petal” pattern (with lower values near the equator and the pole) of turbulence energy density Z^2 in Figure 1(j) inside the termination shock corresponds closely to and is responsible for

the similar distributions of proton and electron temperatures in Figures 1(d) and (e). All three heliospheric boundaries are clearly seen also in the plot of correlation length λ in Figure 1(l).

Figure 2 shows results that are similar to those in Figure 1, but for a period close to the maximum of the current solar cycle 24. The model solar wind inside 40 au was computed in Usmanov et al. (2014) for the boundary conditions on the Sun determined using the synoptic magnetogram of the Wilcox Solar Observatory for Carrington Rotation 2123, 2012 April 28–May 25. The simulated coronal (1–20 solar radii) and solar wind structure (0.3–100 au) are shown in Figures 9 and 11, respectively, in Usmanov et al. (2014). The key difference in this case representative of solar maximum in comparison with the results in Figure 1, is that the wind is now relatively dense and slow at all latitudes. Even though it is more latitudinally uniform, it is no longer axially symmetric and therefore we updated the inner boundary conditions in the course of time relaxation to include solar rotation effects. The termination shock, heliopause and bow shock are now significantly closer to the Sun, the diameter of heliotail is smaller and the heliopause is no longer caving in on the upwind side in the vicinity of the helioequator.

The simulated profiles of flow, magnetic field and turbulence parameters in the “solar minimum” case are shown in Figure 3 along the radial line close to the trajectory of *Voyager 1* ($\theta = 54^\circ 75'$, $\phi = 174^\circ 75'$). The termination shock, heliopause, and bow shock are clearly seen in most of the plots at approx. 105, 140, and 290 au, respectively. The radial speed profile in Figure 3(a) reveals the deceleration of the wind inside the termination shock due to the energy transfer to pickup protons. The speed decrease between 40 and 105 au is about 14% (from 718 to 630 km s⁻¹). The speed drops sharply on the termination shock to ~ 130 km s⁻¹, it decreases then to zero on the heliopause, and only slightly varies in the outer heliosheath and across the bow shock. The magnetic field strength rises steeply on the termination shock and across the inner heliosheath to reach a peak of 0.64 nT at the heliopause. It then gradually decreases to 0.3 nT just downstream of the bow shock. The variations of thermal N_S and pickup proton N_I densities are shown in Figure 3(b). Both densities are relatively small inside the heliosphere and rise sharply in the vicinity of the heliopause. The thermal proton density N_S increases monotonically before the bow shock up to 0.18 cm⁻³. N_I is instead decreasing toward the bow shock after a steep jump near the heliopause. Figure 3(b) shows also the total proton density $N_S + N_I$ and the interstellar hydrogen density N_H . The latter varies only in the outer heliosheath increasing monotonically from the heliopause to the bow shock.

Figure 3(c) shows radial variations of thermal proton temperature $T_S = P_S/k_B N_S$, electron temperature $T_E = P_E/k_B N_E$, pickup proton temperature $T_I = P_I/k_B N_I$, interstellar hydrogen temperature $T_H = P_H/k_B N_H$, and also a mean plasma temperature computed as $\bar{T} = (T_S N_S + T_E N_E + T_I N_I)/(N_S + N_E + N_I)$ (Whang 1998). While the thermal proton and electron temperatures inside the termination shock are $\sim 10^4$ K, the temperature of pickup protons is $\sim 10^7$ K. The same three order of magnitude difference is approximately maintained throughout the inner heliosheath. The importance of pickup protons for the thermal balance of the solar wind plasma is clear from the fact that their contribution causes the mean temperature to differ significantly from that of the thermal electrons and protons. Therefore, all one-fluid heliospheric plasma models (specifically, all the existing three-dimensional global heliospheric models) generate temperatures that cannot be directly compared with observations on

Voyager because the observations do not cover the energy range of pickup protons. In the outer heliosheath, the temperatures of all species are only slightly different and pickup protons become virtually indistinguishable from thermal protons.

The importance of pickup protons for energy balance in the distant solar wind is demonstrated again in Figure 3(d) by comparing radial variations of partial pressures as well as magnetic pressure P_M . The thermal pressure of pickup protons overwhelmingly dominates all other pressure components within the heliopause except for the region just inside the heliopause where the proton and electron pressures steeply rise and the magnetic pressure dominates. At the same time, the turbulence energy density Z^2 quickly drops in this region to further decrease slowly through the outer heliosheath and drop down again to a negligible value at the bow shock. The variations of Z^2 and the correlation length λ in Figure 3(e) are strongly anticorrelated, obviously because of a local conservation law of the form $Z\lambda = \text{const}$ used for specifying the nonlinear terms in the λ equation (Matthaeus et al. 1999). The normalized cross helicity σ_c shown in Figure 3(f) is generally small except for the region just inside the bow shock where, as mentioned above, the gradient of Z^2 along the magnetic field is responsible for the generation of cross helicity.

Figure 3(f) shows also the relative amplitude of magnetic field fluctuations, $\delta B/B \equiv \langle B'^2 \rangle^{1/2}/B = [2\pi\rho(1 - \sigma_D)Z^2/B^2]^{1/2}$. This amplitude is ~ 0.3 in the supersonic solar wind and it drops steeply to below 0.1 at the termination shock. Just outside the heliopause, the turbulence is weak with $\delta B/B = 0.027$. This is in close agreement with the value of 0.023 derived by Burlaga et al. (2015) from the measurements on *Voyager 1*, which is still relatively close to the heliopause. The simulated $\delta B/B$ increases then with distance up to 0.064 before dropping down to ~ 0.005 at the bow shock.

Figure 4 shows radial profiles of the thermal proton density for the two models discussed above: “solar minimum” (0°-model) and “solar maximum” (CR2123-model). The profiles are shown for the two radial lines ($\theta = 54^\circ 75'$, $\phi = 174^\circ 75'$) and ($\theta = 120^\circ 75'$, $\phi = 218^\circ 25'$) close to the trajectories of *Voyager 1* and 2, respectively. The difference of ~ 10 au (~ 2 au) between the profiles for the two locations of the termination shock and heliopause during solar minimum (maximum) conditions confirms that the heliospheric structure is much less asymmetric around solar maximum, when the solar wind is on average slower and more isotropic. The location of the heliospheric interaction boundaries is significantly different for the “minimum” and “maximum” cases: the termination shock and heliopause move in by ~ 20 – 30 au, and the bow shock is shifted inward by 70 – 80 au for solar maximum conditions. The ripples in the “solar maximum” curves result from the periodic (“rotating”) boundary conditions imposed on the inner boundary of 40 au to account for solar rotation in this non-axisymmetric (with respect to the solar rotation axis) case. We note here that the inner heliosheath width ~ 30 – 35 au in Figure 4 is at odds with the statement of Borovikov & Pogorelov (2014) that “no realistic steady-state model ... gives an inner heliosheath width as narrow as ~ 30 au,” which Borovikov and Pogorelov used to justify the hypothesis that *Voyager 1* is moving through a region of temporary penetration by the local interstellar medium.

Figure 5 shows contour plots of the Alfvén Mach number $M_A = u/V_A$, the Mach number computed with respect to the pickup proton sound speed $M = u/C_I$, where $C_I = (\gamma_I P_I/\rho_I)^{1/2}$ and $\gamma_I = 5/3$ is the adiabatic index of pickup protons, and the

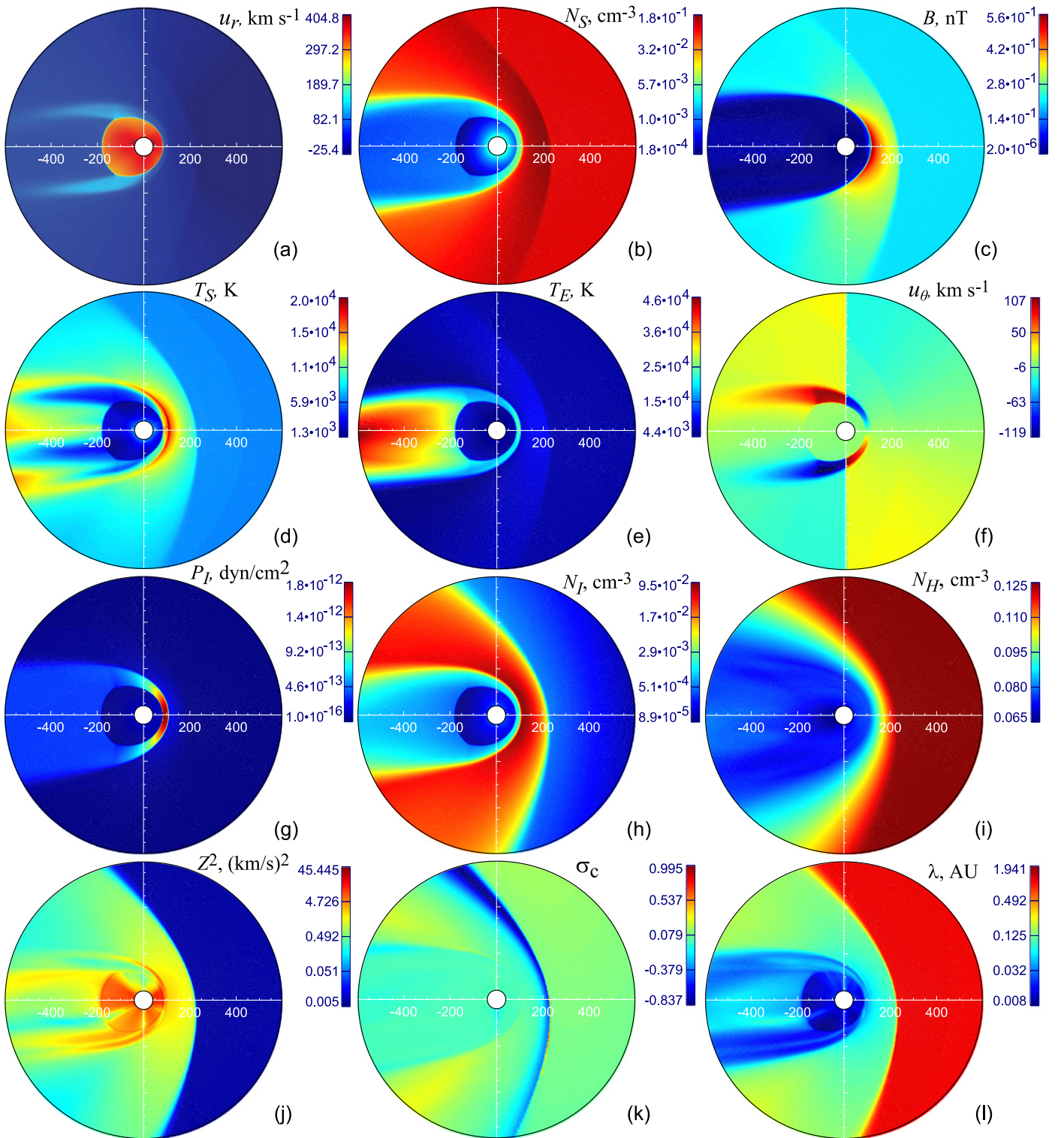


Figure 2. Same as in Figure 1 for the CR2123-model.

plasma beta parameter computed based on the total thermal pressure $\beta_T = 8\pi(P_S + P_I + P_E)/B^2$. The upper (lower) row in Figure 5 shows the plots for the “minimum” (“maximum”) heliospheric model. The heavy white lines trace the locations where the respective parameter is equal to unity. As one would expect, the plasma flow is sub-Alfvénic in the heliosheath in front of the heliosphere. The flow is also sub-Alfvénic in the low-latitude regions of the heliotail that can be seen in

Figure 5(a) for the 0° -model. The front-side sub-Alfvénic region covers similar range of latitudes in both models, but its radial extent, which coincides with the width of the outer heliosheath, is notably larger for the 0° -model. Figures 5(c) and (d) show that the plasma flow is subsonic outside the termination shock up to about the heliopause and also in an outer heliosheath region in front of the heliosphere. The front-side subsonic regions are narrower in latitude and radially

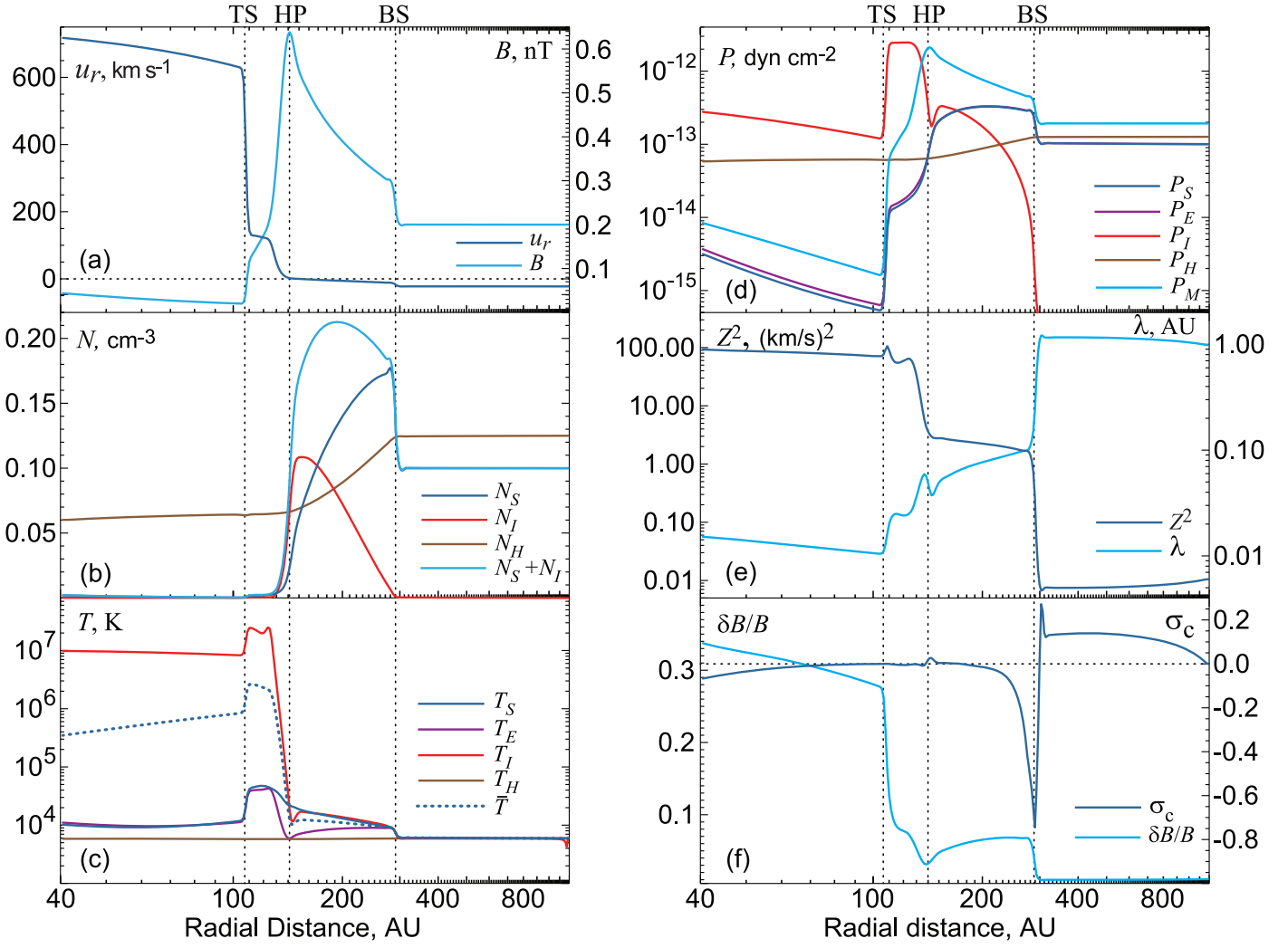


Figure 3. Radial profiles of the flow, magnetic field, and turbulence parameters along the *Voyager 1* trajectory for the 0° -model from 40 au to 1200 au: (a) radial velocity u_r and magnetic field strength B ; (b) thermal proton N_S , pickup proton N_I , interstellar hydrogen N_H , and total proton $N_S + N_I$ densities; (c) proton T_S , electron T_E , pickup proton T_I , interstellar hydrogen T_H , and mean \bar{T} temperatures, where $\bar{T} = (T_S N_S + T_E N_E + T_I N_I) / (N_S + N_E + N_I)$; (d) proton P_S , electron P_E , pickup proton P_I , interstellar hydrogen P_H , and magnetic P_M pressures; (e) turbulent energy density Z^2 and correlation length λ ; (f) cross helicity σ_c and relative amplitude of the magnetic field fluctuations $\delta B/B$. The vertical lines mark the locations of the termination shock, heliopause, and bow shock (TS/HP/BS) at $\sim 105/140/290$ au, respectively.

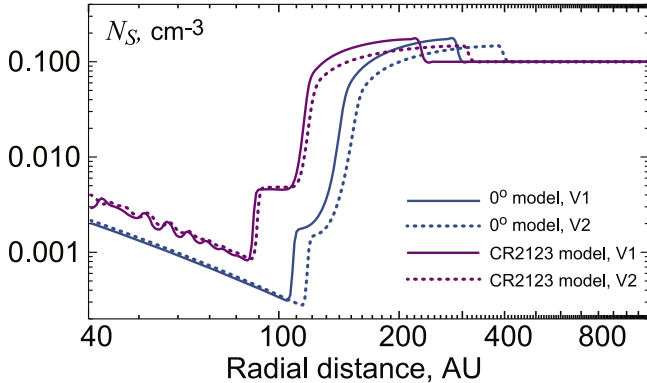


Figure 4. Radial profiles of the thermal proton density N_S along the *Voyager 1* (V1) and *Voyager 2* (V2) trajectories for the 0° -model and CR2123 model.

thinner in comparison with the respective sub-Alfvénic regions. We emphasize that the location of the termination shock coincides perfectly with the $M = 1$ contour, where the Mach number is calculated based on the pickup proton sound speed rather than on the thermal proton sound speed.

The plasma beta parameter β_T shown in Figures 5(e) and (f) is smaller than 1 only in the region between the two white contours that trace the locations with $\beta_T = 1$. While the inner contour closely outlines the heliopause, the strong asymmetry of the outer one (with respect to the upstream direction) is obviously related to the direction of interstellar magnetic field. The assumed orientation of the interstellar field toward the center of the *IBEX* ribbon and its draping around the heliopause lead to a stronger field compression and therefore to lower values of β_T south of the helioequator. Consequently, the outer contour comes closer to the heliopause north of the helioequator. It is important to note that inside the heliopause, β_T is everywhere larger than 1, i.e., the total thermal pressure dominates the magnetic pressure. Together with the fact that the flow inside the heliosphere is predominantly super-Alfvénic (see Figures 5(a)–(b)), that implies that in our simulations the heliospheric magnetic field is not strong enough to produce the separated two-lobe magnetized jets discussed by Opher et al. (2015).

The reason for the inward shift of the termination shock and heliopause can be easily seen in Figure 6 that shows radial variations of the dynamic pressure $P_D = m_p(N_S + N_I)u_r^2$ and the

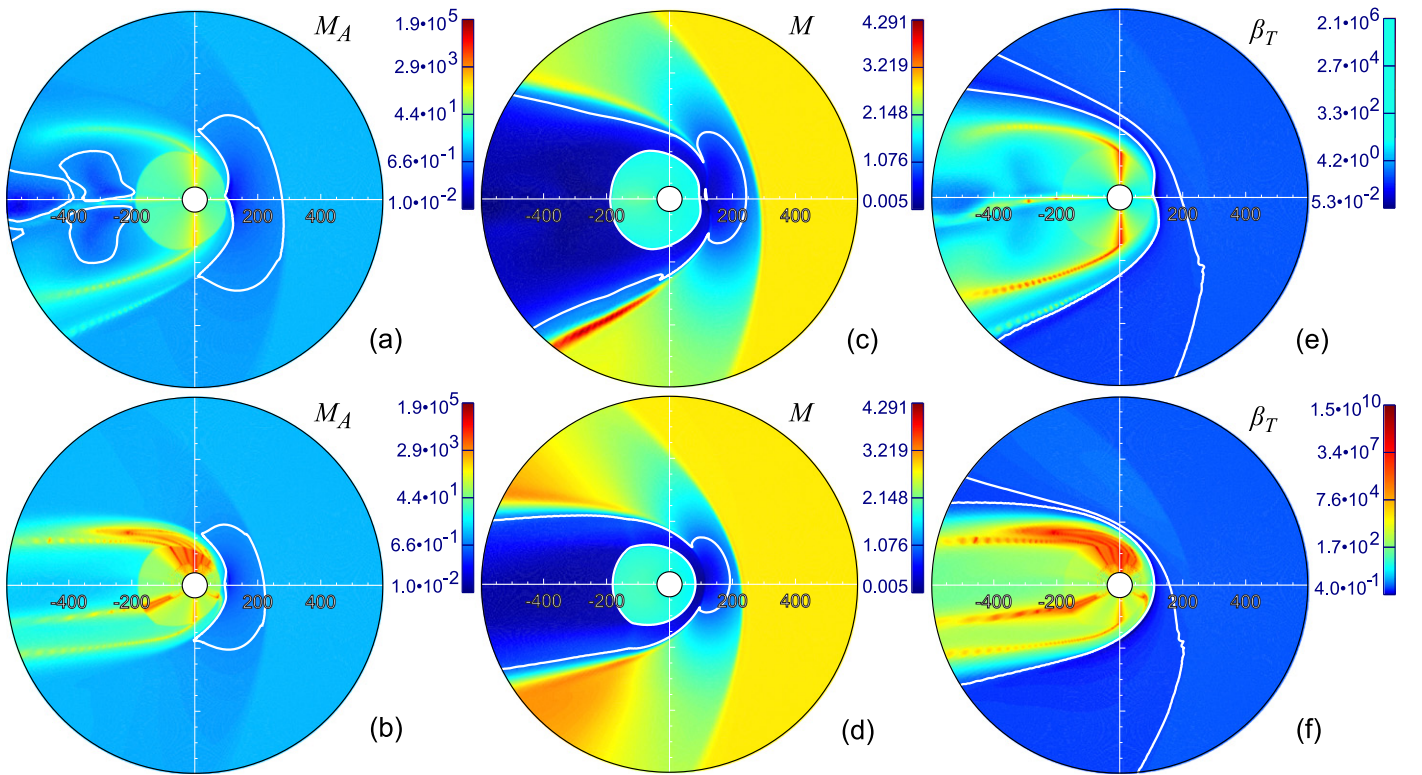


Figure 5. Contour plots of computed non-dimensional parameters in the meridional plane containing the interstellar upwind direction from 40 to 600 au for the 0° -model (upper row) and CR2123-model (lower row): (a)–(b) the Alfvén Mach number $M_A = u/V_A$, (c)–(d) the sonic Mach number $M = u/C_s$, where $C_s = (\gamma_i P_i / \rho_i)^{1/2}$ is the sound speed of pickup protons with the adiabatic index $\gamma_i = 5/3$, and (e)–(f) the plasma beta parameter $\beta_T = 8\pi(P_S + P_I + P_E)/B^2$. The heavy white line in each plot shows the locations where the respective parameter is equal to unity.

total pressure $P_T = P_D + P_S + P_E + P_I + P_M + P_W$, where $P_W = (1 + \sigma_D)\rho Z^2/4$ is the turbulence pressure. Even though the solar wind during solar maximum is generally more dense (as can be seen in Figure 4), its dynamic pressure is notably lower and therefore the pressure balance between the solar wind and interstellar plasma shifts toward the Sun. The figure demonstrates clearly also that inside the termination shock and outside the bow shock P_T is almost equal to P_D , i.e., P_D strongly dominates all other pressure components. In the inner heliosheath, the dominant component is the pressure of pickup protons and in the outer heliosheath, the leading role is played by magnetic field (see Figure 3). We should note here that in addition to pressure forces, the magnetic tension can play an important role in the outer heliospheric dynamics (e.g., Ratkiewicz & McKenzie 2003).

To demonstrate the effects of turbulence and Coulomb collisions on the distribution of proton and electron temperature in the outer heliosphere, Figure 7 shows radial profiles of thermal proton T_S and electron T_E temperatures along the *Voyager 1* trajectory in comparison with the runs without turbulence ($Z^2 = 0$) or Coulomb collisions ($\tau_{SE} = \infty$). It is clear from Figure 7(a) that taking into account turbulence effects significantly changes the distributions of thermal proton and electron temperatures inside the heliosphere. Instead of decreasing with distance, both T_S and T_E increase toward the termination shock. The deviation of the curves for the runs with and without turbulence is also quite pronounced in the inner heliosheath where the level of turbulence is relatively high (Figure 3). In the interstellar plasma beyond the heliopause, Z^2 drops to low values,

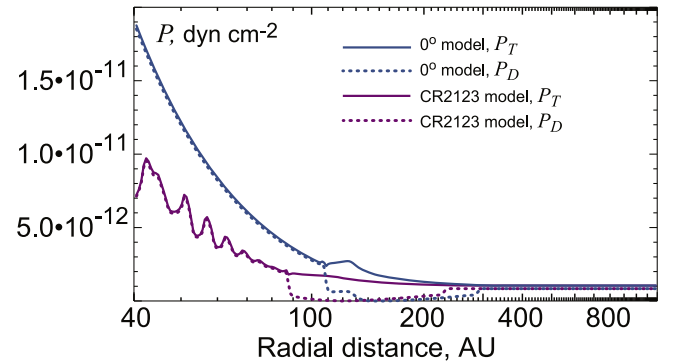


Figure 6. Radial profiles of the dynamic P_D and total P_T pressures along the *Voyager 1* trajectory for the 0° -model and CR2123-model.

especially outside the bow shock, and the impact of turbulence on the temperatures becomes negligible.

The Coulomb collisions affect the distributions of proton and electron temperatures only weakly, except for the region just inside the heliopause and in the outer heliosheath. Because of the presence of pickup protons, the collisions between thermal protons and electrons produce an effect that is opposite to the usual expectation that collisions tend to equalize the temperatures of the interacting species. On the contrary, here the collisions lead to a stronger deviation of the temperature profiles. It can be easily explained by the fact that although the pressures of electron and thermal protons are virtually equal (see Figure 3(d)), their number densities differ by $N_I = N_E - N_S$. In the region just inside the heliopause and in the heliosheath, where the N_I is relatively high, this leads to the stronger difference in temperatures.

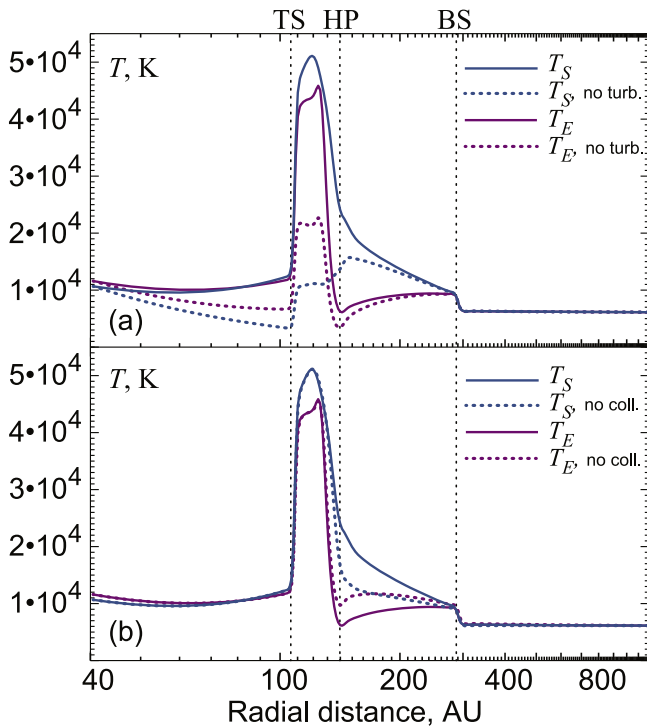


Figure 7. Radial profiles in the 0° -model along the *Voyager 1* trajectory: thermal proton T_S and electron T_E temperatures in comparison with those in the runs with same parameters, but (a) without turbulence ($Z^2 = 0$) or (b) without Coulomb collisions ($\tau_{SE} = \infty$). The vertical lines mark the locations of the termination shock, heliopause and bow shock (TS/HP/BS) at $\sim 105/140/290$ au, respectively.

Figure 8 shows the simulated magnetic field parameters in the spacecraft-centered RTN (Radial-Tangential-Normal) coordinates (Burlaga 1984) along the *Voyager 1* trajectory for the 0° - and CR2123-models. The azimuthal angle $\hat{\lambda}$ and the elevation angle $\hat{\delta}$ characterize the deviation of magnetic field vector from the radial direction at the spacecraft location (see Figure 3 in Burlaga (1984), where the notations for the azimuthal and elevation angles are λ and δ , respectively). In the distant solar wind, where the nominal Parker spiral angle is close to 90° and the magnetic field direction is nearly azimuthal, $\hat{\delta}$ is close to 0° and $\hat{\lambda}$ to -90° or $+90^\circ$. Figure 8(a) shows that for the 0° -model, the simulated $\hat{\delta}$ inside the termination shock is indeed close to 0° and $\hat{\lambda} \approx -90^\circ$. The negative sign of $\hat{\lambda}$ is consistent with the assumed orientation of the source magnetic dipole on the Sun along the solar rotation axis, which results in the positive ($\hat{\lambda} = 90^\circ$) and negative ($\hat{\lambda} = -90^\circ$) azimuthal field component respectively below and above the helioequator. The simulated $\hat{\lambda}$ and $\hat{\delta}$ show no significant variations across the inner heliosheath, where the magnetic field maintains the direction close to the Parker spiral. Inside the outer heliosheath, $\hat{\delta}$ quickly raises to $\sim 25^\circ$, undergoes little changes up to ~ 180 au, and then slowly decreases toward the bow shock where it drops to the unperturbed interstellar value. Meanwhile $\hat{\lambda}$ increases approximately linearly in the outer heliosheath before jumping up by about 20° on the termination shock to reach the unperturbed interstellar value. We note that beyond 150 au we approximate the position of *Voyager 1* by the heliographic latitude and longitude of $34^\circ.8$ and $175^\circ.3$, respectively. Correspondingly, for the assumed interstellar magnetic field direction toward the center of the ENA-ribbon, the undisturbed interstellar values of $\hat{\lambda}$ and $\hat{\delta}$ are -29° and 6° , respectively.

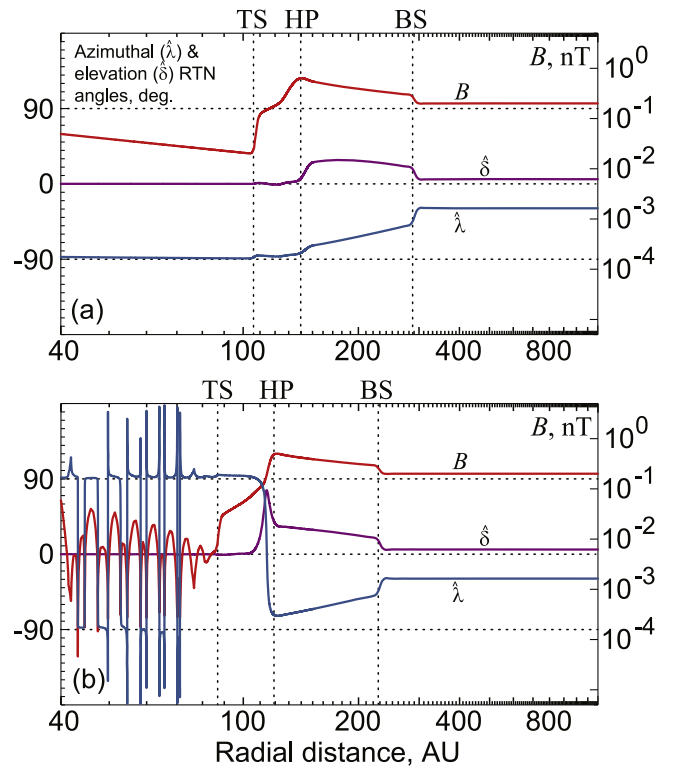


Figure 8. Computed variations along the *Voyager 1* trajectory for (a) the 0° -model and (b) CR2123-model: the magnetic field magnitude B , and the azimuthal ($\hat{\lambda}$) and elevation ($\hat{\delta}$) angles in the spacecraft-centered RTN coordinates (Burlaga 1984). The vertical lines mark the locations of the termination shock, heliopause, and bow shock (TS/HP/BS) at $\sim 105/140/290$ au (a) and $\sim 85/120/230$ au (b), respectively.

The profiles of $\hat{\lambda}$ and $\hat{\delta}$ in Figure 8(a) show that the magnetic field in the outer heliosheath becomes more radial with distance and that $\hat{\lambda}$ increases approximately linearly. The slopes in $\hat{\lambda}$ and $\hat{\delta}$ between 150 and 280 au estimated using *Voyager 1*'s speed of 3.6 au yr^{-1} are about $0^\circ.7 \text{ yr}^{-1}$ and $-0^\circ.1 \text{ yr}^{-1}$, respectively. The simulated variations are qualitatively consistent with the changes in $\hat{\lambda}$ and $\hat{\delta}$ outside the heliopause observed by *Voyager 1* in 2012–2014 (Burlaga & Ness 2014; Burlaga et al. 2015). The simulated slopes are however more shallow in comparison with the respective estimates of $1^\circ.9 \text{ yr}^{-1}$ and $-0^\circ.4 \text{ yr}^{-1}$ obtained from *Voyager 1* data by Burlaga et al. (2015). The shallower slopes lead to a longer time for *Voyager 1* to reach an undisturbed interstellar medium in comparison with the time predicted using a linear extrapolation of the *Voyager* data (Schwadron et al. 2015).

The computed profiles of the magnetic field for the CR2123-model along the *Voyager 1* trajectory are shown in Figure 8(b). The magnetic field in the solar wind inside the termination shock is now much more complex showing numerous sector boundaries, where the azimuthal angle $\hat{\lambda}$ oscillates between $\pm 90^\circ$. The last abrupt change occurs in the solar wind just inside the heliopause. The azimuthal angle $\hat{\lambda}$ rotates from 90° to -73° before increasing linearly toward the bow shock. The slope is about the same as in Figure 8(a) ($0^\circ.8 \text{ yr}^{-1}$). The elevation angle $\hat{\delta}$ inside the termination shock is close to 0° and peaks to $\sim 80^\circ$ simultaneously with the jump in $\hat{\lambda}$ just inside the heliopause. $\hat{\delta}$ decreases approximately linearly in the outer heliosheath with the slope about $-0^\circ.6 \text{ yr}^{-1}$.

The results similar to those in Figure 8, but along the *Voyager 2* trajectory, are shown in Figure 9. Unlike *Voyager 1*, which is

moving northward through the outer heliosphere at an angle of $\sim 35^\circ$ with respect to the helioequatorial plane, *Voyager 2* is traveling into the southern heliosphere at about -30° heliolatitude. As our 0° -model assumes a source magnetic dipole on the Sun aligned with the solar rotation axis, the simulated magnetic field direction inside the termination shock in Figure 9(a) is opposite to that in Figure 8(a) and close to 90° . $\hat{\lambda}$ changes its sign abruptly at the heliopause and shows little variation across the outer heliosheath. The elevation angle $\hat{\delta}$ also shows no significant variations except for a peak at the heliopause. Beyond 125 au, we approximate the position of *Voyager 2* by the heliographic latitude -32.8° and longitude 218.6° . The undisturbed interstellar values of $\hat{\lambda}$ and $\hat{\delta}$ are therefore -103° and 34° , respectively.

The magnetic field in the outer heliosheath is the interstellar magnetic field draped around the heliopause by the interstellar plasma flow. The effect of draping has been studied recently using analytical models by Whang (2010b), Schwadron et al. (2014), Röken et al. (2015), Isenberg et al. (2015). Assuming a potential plasma flow around the heliopause of a pre-defined shape, Isenberg et al. (2015) obtained analytical solutions for a passive frozen-in magnetic field and the interstellar magnetic field directed toward the center of the *IBEX* ribbon. The variations of the magnetic field parameters computed by Isenberg et al. (2015) along the *Voyager 1* trajectory show that $\hat{\lambda}$ increases and $\hat{\delta}$ decreases with distance in qualitative agreement with the *Voyager 1* observations (Burlaga & Ness 2014; Burlaga et al. 2015) and with our results shown in Figure 8. Similarly, our profiles along the *Voyager 2* trajectory shown in Figure 9 are in agreement with Isenberg et al.'s prediction that the magnetic field direction measured by *Voyager 2* beyond the heliopause will not be significantly different from the direction of the unperturbed interstellar magnetic field.

4. SUMMARY AND FUTURE DEVELOPMENTS

We have developed a four-fluid three-dimensional MHD global heliospheric model that incorporates turbulence transport and pickup protons as a separate fluid. Turbulence transport equations are coupled and solved simultaneously with the mean-flow equations. Unique features of the model presented in this paper are:

(1) A three-fluid description for the plasmas of solar wind and interstellar medium with separate energy equations for thermal protons, electrons, and pickup protons.

(2) The built-in turbulence transport equations for turbulence energy, normalized cross helicity and correlation length. The equations have been derived using Reynolds decomposition and turbulence phenomenologies developed previously (e.g., Breech et al. 2008; Usmanov et al. 2014).

(3) The solar wind model (Usmanov et al. 2014) that supplies the boundary conditions at 40 au and, as a result, the heliospheric structure is computed all the way from the coronal base to the unperturbed interstellar medium.

Using the model, we have computed the distributions of plasma, magnetic field, and turbulence quantities throughout the heliosphere for representative solar minimum and maximum conditions. We have shown that the thermal pressure of pickup protons overwhelmingly dominates all other pressure components within the heliopause except the region just inside the heliopause. By comparing simulation results of the runs with and without turbulence (i.e., terms with Z^2 and \dot{E}_{PI} were set to zero), we showed that the effect of turbulence is to change significantly the distribution of thermal proton and electron temperatures inside the heliosphere. A similar comparison of the runs with and without

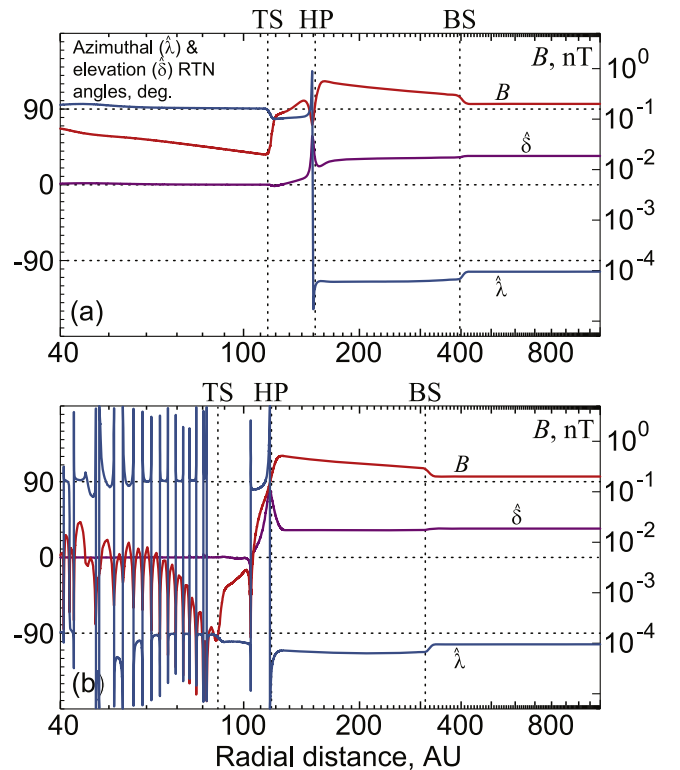


Figure 9. Same simulated parameters as in Figure 8 along the *Voyager 2* trajectory for (a) the 0° -model and (b) CR2123-model. The vertical lines mark the locations of the termination shock, heliopause, and bow shock (TS/HP/BS) at $\sim 115/150/400$ au (a) and $\sim 85/115/310$ au (b), respectively.

Coulomb collisions (i.e., $\tau_{SE} = \infty$) demonstrated that the effect of Coulomb collisions on the thermal proton and electron temperatures is relatively weak except in the region just inside the heliopause and in the outer heliosheath.

We have compared our results with *Voyager 1* observations just outside the heliopause. We found that the computed level of magnetic field fluctuations matches closely the one inferred from *Voyager 1* measurements by Burlaga et al. (2015). The computed variations of magnetic field parameters in the outer heliosheath are in qualitative agreement with the *Voyager 1* observations (Burlaga et al. 2015) and with the results from the analytical model of magnetic field draping around the heliopause by Isenberg et al. (2015). Our results support the prediction of Isenberg et al. (2015) that the direction of the magnetic field measured by *Voyager 2* in the outer heliosheath will not be significantly different from the direction of the unperturbed interstellar magnetic field.

Knowledge of spatial distribution of turbulence intensity is an important input for computations of energetic particle propagation throughout the heliosphere. Since the heliospheric model presented in this study provides not only mean-flow plasma and magnetic field parameters, but also the turbulence quantities, which are necessary for calculation of diffusion coefficients, the model can be useful in studies of solar energetic particles and solar modulation of galactic cosmic rays (see, e.g., Florinski et al. 2013).

To outline possible future development, we list the main limitations of the present analysis.

(1) One weakness is the use of a simple one-fluid model for interstellar hydrogen with the source terms due to charge exchange described by simplified formulas (Holzer 1972). It is

an obvious future development to implement more elaborate formulas for charge exchange terms derived by McNutt et al. (1998, 1999), a multi-fluid description of hydrogen as suggested by Pauls et al. (1995) and Zank et al. (1996), or even a kinetic formalism based on a Monte Carlo approach (Malama 1991; Heerikhuisen et al. 2006).

(2) The present formulation neglects the effects of shear driving of turbulence, which are included in the Usmanov et al. (2014) solar wind model by implementing an eddy viscosity approximation for the Reynolds stress tensor and turbulent electric field. We plan to add these effects in our future studies.

(3) Unlike the supersonic solar wind, where fluctuations are predominantly incompressible, the fluctuations observed by *Voyager 1* and 2 in the inner heliosheath appear to be highly compressible (Burlaga et al. 2006; Burlaga & Ness 2009). Thus, it is very desirable to extend the turbulence model to account for compressible fluctuations.

(4) There are a number of parameters in the present model that we treat as constants: the charge exchange cross section σ , the normalized energy difference σ_D , the isotropization parameter f_D , the fraction of turbulent energy absorbed by protons f_p . In fact, all the parameters should be rather considered as functions of plasma and magnetic field properties: σ should depend on the relative velocity thermal protons and hydrogen atoms (e.g., Fite et al. 1962; Maher & Tinsley 1977; Lindsay & Stebbings 2005), σ_D should be described by an evolution equation as suggested, e.g., by Zhou & Matthaeus (1990), Tu & Marsch (1993), Yokoi et al. (2008), Zank et al. (2012), f_D should be a function of the flow and turbulence parameters (Isenberg et al. 2003; Isenberg 2005; see also the discussion in Smith et al. 2006), and f_p likely depends on heliocentric distance (Cranmer et al. 2009) and the local plasma conditions and turbulence properties.

(5) Although we solve time-dependent Equations (24) and include the effect of solar rotation in the inner boundary conditions, solar cycle effects are not explicitly included in the present study. We leave for work a global long-term time-dependent simulation of the entire heliosphere from the coronal base to the interstellar medium.

We gratefully acknowledge Len Burlaga for invaluable discussions during the course of this study. This work was supported in part by NASA LWS program (grants NNX13AR42G and NNX15AB88G), NASA Heliophysics Grand Challenges Research program (grant NNX14AI63G), and the Solar Probe Plus ISIS project under subcontract D99031L. Supercomputer time allocations were provided by the NASA High-End Computing (HEC) Program awards SMD-14-4848 and SMD-15-5715 through the NASA Advanced Supercomputing (NAS) Division at the Ames Research Center and the NASA Center for Climate Simulation (NCCS) at the Goddard Space Flight Center.

APPENDIX THE INTEGRATED SYSTEM OF EQUATIONS IN THE COMPONENT FORM

Introducing the following non-dimensional parameters: the Strouhal number $S_h = u_0 T_0 / L_0$, the Euler number $E_u = P_0 / \rho_0 u_0^2$, the Froude number $F_r = u_0^2 L_0 / GM_\odot$, and the Alfvén

Mach number $M_A = u_0 (4\pi\rho_0)^{1/2} / B_0$, where L_0 , T_0 , ρ_0 , u_0 , B_0 , and P_0 are units of length, time, density, velocity, magnetic field, and pressure, respectively, the integrated system of Equations (1), (13)–(15), (18)–(20), (5), (16)–(17), and (10)–(12) can be re-written in spherical coordinates on the logarithmically spaced grid, $r' = \ln(r/r_0)$, in the following non-dimensional quasi-conservation form

$$\frac{\partial \mathbf{W}}{\partial t} = \frac{\partial \mathbf{F}}{\partial r'} + \frac{\partial \mathbf{G}}{\partial \theta} + \frac{\partial \mathbf{H}}{\partial \phi} + \mathbf{S}, \quad (24)$$

where

$$\mathbf{W} = \begin{pmatrix} r^3 \rho_S \\ r^3 \rho u_r \\ r^3 \rho u_\theta \\ r^3 \rho u_\phi \\ r^2 B_r \\ r^2 B_\theta \\ r^2 B_\phi \\ r^3 P_S^{1/\gamma} \\ r^3 Z^2 \\ r^3 Z^2 \sigma_c \\ r^3 Z \lambda \\ r^3 \rho_I \\ r^3 P_I^{3/5} \\ r^3 P_E^{1/\gamma} \\ r^3 \rho_H \\ r^3 \rho_H u_{Hr} \\ r^3 \rho_H u_{H\theta} \\ r^3 \rho_H u_{H\phi} \\ r^3 \rho_H E_H \end{pmatrix}, \quad \mathbf{F} = -S_h \begin{pmatrix} r^2 \rho_S u_r \\ r^2 \rho (u_r^2 + \bar{P} - \eta V_{Ar}^2) \\ r^2 \rho (u_r u_\theta - \eta V_{Ar} V_{A\theta}) \\ r^2 \rho (u_r u_\phi - \eta V_{Ar} V_{A\phi}) \\ 0 \\ r (u_r B_\theta - u_\theta B_r) \\ -r (u_\phi B_r - u_r B_\phi) \\ r^2 u_r P_S^{1/\gamma} \\ r^2 Z^2 (u_r - \sigma_c V_{Ar}) \\ r^2 Z^2 (\sigma_c u_r - V_{Ar}) \\ r^2 Z \lambda u_r \\ r^2 \rho_I u_r \\ r^2 u_r P_I^{3/5} \\ r^2 u_r P_E^{1/\gamma} \\ r^2 \rho_H u_{Hr} \\ r^2 \rho_H (u_{Hr}^2 + \bar{P}_H) \\ r^2 \rho_H u_{Hr} u_{H\theta} \\ r^2 \rho_H u_{Hr} u_{H\phi} \\ r^2 \rho_H u_{Hr} (E_H + \bar{P}_H) \end{pmatrix},$$

$$\mathbf{G} = -S_h \begin{pmatrix} r^2 \rho_S u_\theta \\ r^2 \rho (u_r u_\theta - \eta V_{Ar} V_{A\theta}) \\ r^2 \rho (u_\theta^2 + \bar{P} - \eta V_{A\theta}^2) \\ r^2 \rho (u_\theta u_\phi - \eta V_{A\theta} V_{A\phi}) \\ -r (u_r B_\theta - u_\theta B_r) \\ 0 \\ r (u_\theta B_\phi - u_\phi B_\theta) \\ r^2 u_\theta P_S^{1/\gamma} \\ r^2 Z^2 (u_\theta - \sigma_c V_{A\theta}) \\ r^2 Z^2 (\sigma_c u_\theta - V_{A\theta}) \\ r^2 Z \lambda u_\theta \\ r^2 \rho_I u_\theta \\ r^2 u_\theta P_I^{3/5} \\ r^2 u_\theta P_E^{1/\gamma} \\ r^2 \rho_H u_{H\theta} \\ r^2 \rho_H u_{Hr} u_{H\theta} \\ r^2 \rho_H (u_{H\theta}^2 + \bar{P}_H) \\ r^2 \rho_H u_{H\theta} u_{H\phi} \\ r^2 \rho_H u_{H\theta} (E_H + \bar{P}_H) \end{pmatrix}, \quad \mathbf{H} = -\frac{S_h}{\sin \theta} \begin{pmatrix} r^2 \rho_S u_\phi \\ r^2 \rho (u_r u_\phi - \eta V_{Ar} V_{A\phi}) \\ r^2 \rho (u_\theta u_\phi - \eta V_{A\theta} V_{A\phi}) \\ r^2 \rho (u_\phi^2 + \bar{P} - \eta V_{A\phi}^2) \\ r (u_\phi B_r - u_r B_\phi) \\ -r (u_\theta B_\phi - u_\phi B_\theta) \\ 0 \\ r^2 u_\phi P_S^{1/\gamma} \\ r^2 Z^2 (u_\phi - \sigma_c V_{A\phi}) \\ r^2 Z^2 (\sigma_c u_\phi - V_{A\phi}) \\ r^2 Z \lambda u_\phi \\ r^2 \rho_I u_\phi \\ r^2 u_\phi P_I^{3/5} \\ r^2 u_\phi P_E^{1/\gamma} \\ r^2 \rho_H u_{H\phi} \\ r^2 \rho_H u_{Hr} u_{H\phi} \\ r^2 \rho_H u_{H\theta} u_{H\phi} \\ r^2 \rho_H (u_{H\phi}^2 + \bar{P}_H) \\ r^2 \rho_H u_{H\phi} (E_H + \bar{P}_H) \end{pmatrix},$$

$$\begin{aligned}
& \left. \begin{aligned}
& -r^2 \rho_S u_\theta \cot \theta - r^3 \hat{q}_{\text{ex}1} \\
& r^2 \rho [u_\theta^2 + u_\phi^2 - 1/(F_r r) + 2\bar{P} - \eta(V_{A\theta}^2 + V_{A\phi}^2) - \cot \theta (u_r u_\theta - \eta V_{Ar} V_{A\theta})] \\
& \quad - r^3 [\hat{q}_T (u_r - u_{Hr}) - \hat{q}_{\text{ph}} u_r] - r^3 \mathbf{B}_r \nabla \cdot \mathbf{B} / M_A^2 \\
& -r^2 \rho [u_r u_\theta - \eta V_{Ar} V_{A\theta} + \cot \theta (u_\theta^2 - u_\phi^2 - \eta(V_{A\theta}^2 - V_{A\phi}^2))] \\
& \quad - r^3 [\hat{q}_T (u_\theta - u_{H\theta}) - \hat{q}_{\text{ph}} u_\theta] - r^3 \mathbf{B}_\theta \nabla \cdot \mathbf{B} / M_A^2 \\
& -r^2 \rho [u_r u_\phi - \eta V_{Ar} V_{A\phi} + 2 \cot \theta (u_\theta u_\phi - \eta V_{A\theta} V_{A\phi})] \\
& \quad - r^3 [\hat{q}_T (u_\phi - u_{H\phi}) - \hat{q}_{\text{ph}} u_\phi] - r^3 \mathbf{B}_\phi \nabla \cdot \mathbf{B} / M_A^2 \\
& r \cot \theta (u_r \mathbf{B}_\theta - u_\theta \mathbf{B}_r) - r^2 u_r \nabla \cdot \mathbf{B} \\
& -r^2 u_\theta \nabla \cdot \mathbf{B} \\
& -r^2 u_\phi \nabla \cdot \mathbf{B} \\
& -r^2 P_S^{1/\gamma} \left\{ u_\theta \cos \theta + \frac{r}{\gamma} \left[\frac{\hat{q}_{\text{ex}1}}{\rho_S} + (\gamma - 1) \left(\frac{P_S - P_E}{P_S \tau_{SE} S_h} - f_p \frac{\alpha f^+(\sigma_c) \rho Z^3}{2 \lambda P_S E_u} \right) \right] \right\} \\
& -r^2 \left\{ Z^2 (u_\theta - \sigma_c V_{A\theta}) \cot \theta - r \left[\frac{Z^2}{2} ((1 - \sigma_D) \nabla \cdot \mathbf{u} + 2 \sigma_D \hat{\mathbf{B}} \cdot (\hat{\mathbf{B}} \cdot \nabla) \mathbf{u} - 4 \sigma_c \nabla \cdot \mathbf{V}_A \right. \right. \\
& \quad \left. \left. - \frac{1}{\rho} (2 \hat{q}_T (1 + \sigma_D) + \hat{q}_{\text{ph}} (1 - \sigma_D)) \right) - \frac{\alpha f^+(\sigma_c) Z^3}{\lambda} + \dot{E}_{PI} + \frac{Z^2 \sigma_c \nabla \cdot \mathbf{B}}{M_A \rho^{1/2}} \right\} \\
& -r^2 \left\{ Z^2 (\sigma_c u_\theta - V_{A\theta}) \cot \theta - r \left[\frac{Z^2}{2} (\sigma_c \nabla \cdot \mathbf{u} + 2 \sigma_D \hat{\mathbf{B}} \cdot (\hat{\mathbf{B}} \cdot \nabla) \mathbf{V}_A \right. \right. \\
& \quad \left. \left. - 4 \nabla \cdot \mathbf{V}_A - \frac{\sigma_c}{\rho} (2 \hat{q}_T + \hat{q}_{\text{ph}}) \right) - \frac{\alpha f^-(\sigma_c) Z^3}{\lambda} + \frac{(1 - \sigma_D) Z^2 \nabla \cdot \mathbf{B}}{M_A \rho^{1/2}} \right\} \\
& -r^2 Z \lambda \left\{ u_\theta \cot \theta - \frac{r}{4} \left[(3 - \sigma_D) \nabla \cdot \mathbf{u} + 2 \sigma_D \hat{\mathbf{B}} \cdot (\hat{\mathbf{B}} \cdot \nabla) \mathbf{u} - \frac{1}{\rho} (2 \hat{q}_T (1 + \sigma_D) \right. \right. \\
& \quad \left. \left. + \hat{q}_{\text{ph}} (1 - \sigma_D)) \right] \right\} + r^3 \lambda \left[\sigma_c (\mathbf{V}_A \cdot \nabla) Z + \frac{Z}{2 \rho^{1/2}} (\mathbf{V}_A \cdot \nabla) (\sigma_c \rho^{1/2}) \right] \\
& -r^2 \rho_I u_\theta \cot \theta + r^3 (\hat{q}_{\text{ex}1} + \hat{q}_{\text{ph}}) \\
& -r^2 P_I^{3/5} \left\{ u_\theta \cot \theta - \frac{r}{5 P_I E_u} \left[\hat{q}_T \left(3 \bar{P}_H + (\mathbf{u} - \mathbf{u}_H)^2 + \frac{(1 + \sigma_D) Z^2}{2} \right) \right. \right. \\
& \quad \left. \left. - 3 \hat{q}_{\text{ex}2} P_I E_u / \rho_I - \rho \dot{E}_{PI} \right] \right\} \\
& -r^2 P_E^{1/\gamma} \left\{ u_\theta \cot \theta - \frac{r(\gamma - 1)}{\gamma P_E E_u} \left[\hat{q}_{\text{ph}} \varepsilon - \frac{(P_E - P_S) E_u}{\tau_{SE} S_h} + (1 - f_p) \frac{\alpha f^+(\sigma_c) \rho Z^3}{2 \lambda} \right] \right\} \\
& -r^2 \rho_H u_{H\theta} \cot \theta - r^3 \hat{q}_T \\
& r^2 \rho_H [u_{H\theta}^2 + u_{H\phi}^2 - (1 - \mu_H)/(F_r r) + 2\bar{P}_H - \cot \theta u_{Hr} u_{H\theta}] - r^3 \hat{q}_T u_{Hr} \\
& -r^2 \rho_H [u_{Hr} u_{H\theta} + \cot \theta (u_{H\theta}^2 - u_{H\phi}^2)] - r^3 \hat{q}_T u_{H\theta} \\
& -r^2 \rho_H (u_{Hr} u_{H\phi} + 2 \cot \theta u_{H\theta} u_{H\phi}) - r^3 \hat{q}_T u_{H\phi} \\
& -r^2 \rho_H u_{H\theta} (E_H + \bar{P}_H) \cot \theta - r^3 \hat{q}_T E_H - r \rho_H (1 - \mu_H) u_{Hr} / F_r
\end{aligned}
\right.
\end{aligned}$$

and all the dependent variables are normalized to their respective units, in particular, $\rho_S = N_S m_p / \rho_0$ and $\rho_I = N_I m_p / \rho_0$. Other quantities are the total density $\rho = \rho_S + \rho_I$, the non-dimensional Alfvén velocity components $V_{Ar, \theta, \phi} = B_{r, \theta, \phi} / M_A \rho^{1/2}$, $\eta = 1 + \sigma_D Z^2 / 2 V_A^2$, where $V_A^2 = V_{Ar}^2 + V_{A\theta}^2 + V_{A\phi}^2$, the total non-dimensional pressure per unit mass

$$\bar{P} = \frac{(P_S + P_E + P_I) E_u}{\rho} + \frac{V_A^2}{2} + \frac{(1 + \sigma_D) Z^2}{4},$$

and the total non-dimensional energy and thermal pressure of interstellar hydrogen per unit mass

$$E_H = \frac{u_H^2}{2} + \frac{3 P_H E_u}{2 \rho_H}, \quad \bar{P}_H = \frac{P_H E_u}{\rho_H}.$$

In the above equations, $\varepsilon = \varepsilon_0 / m_p u_0^2$ is the non-dimensional average energy of photoelectrons, $\hat{q}_T = \hat{q}_{\text{ex}1} + \hat{q}_{\text{ex}2} + \hat{q}_{\text{ph}}$, where $\hat{q}_{\text{ex}1, \text{ex}2, \text{ph}} = q_{\text{ex}1, \text{ex}2, \text{ph}} m_p L_0 / u_0 \rho_0$ are the non-dimensional production rates of pickup protons from interstellar hydrogen atoms by charge exchange with solar wind protons

\hat{q}_{ex1} , with interstellar pickup protons \hat{q}_{ex2} , and by photoionization \hat{q}_{ph} . \dot{E}_{PI} is here the non-dimensional energy of pickup protons converted into turbulence energy

$$\dot{E}_{PI} = f_D \frac{uV_A}{\rho} (\hat{q}_{ex1} + \hat{q}_{ex2} + \hat{q}_{ph}).$$

In total, Equation (24) consists of 19 scalar equations for 19 scalar dependent variables. Equation (24) is written in the form that does not assume that $\nabla \cdot \mathbf{B} = 0$ and, as a result, includes terms with $\nabla \cdot \mathbf{B}$. Note that the transformation to the logarithmic grid is performed by substituting $\partial/\partial r = (1/r)\partial/\partial r'$ and that in addition to the standard terms with $\nabla \cdot \mathbf{B}$ introduced following Powell (1994) into the momentum and induction equation, the appropriate $\nabla \cdot \mathbf{B}$ -terms appear also in the Z^2 and $Z^2\sigma_c$ equations. The equation for $Z\lambda$ in (24) is the result of combining Equations (18) and (20) and using the $\alpha = 2\beta$ relation between the Kármán–Taylor constants.

REFERENCES

- Baranov, V. B., Lebedev, M. G., & Malama, Y. G. 1991, *ApJ*, 375, 347
- Baranov, V. B., & Malama, Y. G. 1993, *JGR*, 98, 15157
- Borovikov, S. N., & Pogorelov, N. V. 2014, *ApJL*, 783, L16
- Borrmann, T., & Fichtner, H. 2005, *AdSpR*, 35, 2091
- Breech, B., Matthaeus, W. H., Cranmer, S. R., Kasper, J. C., & Oughton, S. 2009, *JGR*, 114, A09103
- Breech, B., Matthaeus, W. H., Minnie, J., et al. 2008, *JGR*, 113, A08105
- Burlaga, L. F. 1984, *SSRv*, 39, 255
- Burlaga, L. F., Florinski, V., & Ness, N. F. 2015, *ApJL*, 804, L31
- Burlaga, L. F., & Ness, N. F. 2009, *ApJ*, 703, 311
- Burlaga, L. F., & Ness, N. F. 2014, *ApJL*, 795, L19
- Burlaga, L. F., Ness, N. F., & Acuña, M. H. 2006, *ApJ*, 642, 584
- Burlaga, L. F., Ness, N. F., Belcher, J. W., & Whang, Y. C. 1996, *JGR*, 101, 15523
- Chalov, S. V., Alexashov, D. B., & Fahr, H. J. 2006, *AstL*, 32, 206
- Cranmer, S. R., Matthaeus, W. H., Breech, B. A., & Kasper, J. C. 2009, *ApJ*, 702, 1604
- Detman, T. R., Intriligator, D. S., Dryer, M., et al. 2011, *JGR*, 116, A03105
- Fahr, H. J., Kausch, T., & Scherer, H. 2000, *A&A*, 357, 268
- Fisk, L. A., & Goldstein, M. L. 1976, On the assimilation of interstellar ions into the solar wind, (unpublished manuscript)
- Fite, W. L., Smith, A. C. H., & Stebbings, R. F. 1962, *RSPSA*, 268, 527
- Florinski, V., Ferreira, S. E. S., & Pogorelov, N. V. 2013, *SSRv*, 176, 147
- Funsten, H. O., Allegrini, F., Crew, G. B., et al. 2009, *Sci*, 326, 964
- Funsten, H. O., DeMajistre, R., Frisch, P. C., et al. 2013, *ApJ*, 776, 30
- Fuselier, S. A., Allegrini, F., Funsten, H. O., et al. 2009, *Sci*, 326, 962
- Gamayunov, K. V., Zhang, M., Pogorelov, N. V., Heerikhuisen, J., & Rassoul, H. K. 2012, *ApJ*, 757, 74
- Gottlieb, S., Shu, C.-W., & Tadmor, E. 2001, *SIAMR*, 43, 89
- Grygorczuk, J., Gzechowski, A., & Grzedziński, S. 2014, *ApJL*, 789, L43
- Hartle, R. E., & Sturrock, P. A. 1968, *ApJ*, 151, 1155
- Heerikhuisen, J., Florinski, V., & Zank, G. P. 2006, *JGR*, 111, A06110
- Holzer, T. E. 1972, *JGR*, 77, 5407
- Hundhausen, A. J. 1972, *Coronal Expansion and Solar Wind* (Berlin: Springer)
- Isenberg, P. A. 1986, *JGR*, 91, 9965
- Isenberg, P. A. 2005, *ApJ*, 623, 502
- Isenberg, P. A., Forbes, T. G., & Möbius, E. 2015, *ApJ*, 805, 153
- Isenberg, P. A., Smith, C. W., & Matthaeus, W. H. 2003, *ApJ*, 592, 564
- Isenberg, P. A., Smith, C. W., Matthaeus, W. H., & Richardson, J. D. 2010, *ApJ*, 719, 716
- Izmodenov, V., Alexashov, D. B., & Myasnikov, A. 2005, *A&A*, 437, L35
- Izmodenov, V. V., Alexashov, D. B., & Ruderman, M. S. 2014, *ApJL*, 795, L7
- Izmodenov, V. V., Malama, Y. G., Ruderman, M. S., et al. 2009, *SSRv*, 146, 329
- Kurganov, A., & Levy, D. 2000, *SIAM J. Sci. Comput.*, 22, 1461
- Lallement, R., Quémerais, E., Koutroumpa, D., et al. 2010, in *AIP Conf. Proc.*, Twelfth Int. Solar Wind Conf. 1216, ed. M. Maksimovic et al. (Melville, NY: AIP), 555
- Lee, M. A., & Ip, W.-H. 1987, *JGR*, 92, 11041
- Linde, T. J. 1998, PhD thesis, Univ. Michigan
- Lindsay, B. G., & Stebbings, R. F. 2005, *JGR*, 110, A12213
- Maher, L. J., & Tinsley, B. A. 1977, *JGR*, 82, 689
- Malama, Y. G. 1991, *Ap&SS*, 176, 21
- Malama, Y. G., Izmodenov, V. V., & Chalov, S. V. 2006, *A&A*, 445, 693
- Matthaeus, W. H., & Goldstein, M. L. 1982, *JGR*, 87, 6011
- Matthaeus, W. H., Minnie, J., Breech, B., et al. 2004, *GeoRL*, 31, L12803
- Matthaeus, W. H., Zank, G. P., Smith, C. W., & Oughton, S. 1999, *PhRvL*, 82, 3444
- McComas, D. J., Alexashov, D., Bzowski, M., et al. 2012, *Sci*, 336, 1291
- McComas, D. J., Allegrini, F., Bochsler, P., et al. 2009, *Sci*, 326, 959
- McComas, D. J., Dayeh, M. A., Funsten, H. O., Livadiotis, G., & Schwadron, N. A. 2013, *ApJ*, 771, 77
- McNutt, R. L., Lyon, J., & Goodrich, C. C. 1998, *JGR*, 103, 1905
- McNutt, R. L., Lyon, J., & Goodrich, C. C. 1999, *JGR*, 104, 14803
- Opher, M., Alouani-Bibi, F., Tóth, G., et al. 2009, *Natur*, 462, 1036
- Opher, M., Drake, J. F., Zieger, B., & Gombosi, T. I. 2015, *ApJL*, 800, L28
- Opher, M., Liewer, P. C., Gombosi, T. I., et al. 2003, *ApJL*, 591, L61
- Pauls, H. L., & Zank, G. P. 1997, *JGR*, 102, 19779
- Pauls, H. L., Zank, G. P., & Williams, L. L. 1995, *JGR*, 100, 21595
- Pogorelov, N. V., & Matsuda, T. 1998, *JGR*, 103, 237
- Pogorelov, N. V., Suess, S. T., Borovikov, S. N., et al. 2013, *ApJ*, 772, 2
- Pogorelov, N. V., Zank, G. P., & Ogino, T. 2006, *ApJ*, 644, 1299
- Powell, K. G. 1994, An Approximate Riemann Solver for Magnetohydrodynamics, Tech. Rep. ICASE No. 94-24 (Hampton, VA: Institute for Computer Applications in Science and Engineering)
- Provnorkova, E., Opher, M., Izmodenov, V. V., Richardson, J. D., & Tóth, G. 2014, *ApJ*, 794, 29
- Ratkiewicz, R., Barnes, A., Molvik, G. A., et al. 1998, *A&A*, 335, 363
- Ratkiewicz, R., & Ben-Jaffel, L. 2002, *JGR*, 107, 1007
- Ratkiewicz, R., & McKenzie, J. F. 2003, *JGR*, 108, 1071
- Röken, C., Kleimann, J., & Fichtner, H. 2015, *ApJ*, 805, 173
- Schwadron, N. A., Adams, F. C., Christian, E. R., et al. 2014, *Sci*, 343, 988
- Schwadron, N. A., Richardson, J. D., Burlaga, L. F., McComas, D. J., & Möbius, E. 2015, *ApJL*, 813, L20
- Smith, C. W., Isenberg, P. A., Matthaeus, W. H., & Richardson, J. D. 2006, *ApJ*, 638, 508
- Smith, C. W., Isenberg, P. A., Matthaeus, W. H., et al. 2004, in *AIP Proc.* 719, Physics of the Outer Heliosphere, ed. V. Florinski, N. V. Pogorelov, & G. P. Zank (Melville, NY: American Institute of Physics), 359
- Smith, C. W., Matthaeus, W. H., Zank, G. P., et al. 2001, *JGR*, 106, 8253
- Tu, C.-Y., & Marsch, E. 1993, *JGR*, 98, 1257
- Usmanov, A. V. 1993, *SoPh*, 146, 377
- Usmanov, A. V. 1996, in *AIP Conf. Proc.*, 382 Solar Wind Conf. Eight Int., ed. D. Winterhalter et al. (Woodbury, NY: AIP), 141
- Usmanov, A. V., & Goldstein, M. L. 2003, *JGR*, 108, 1354
- Usmanov, A. V., & Goldstein, M. L. 2006, *JGR*, 111, A07101
- Usmanov, A. V., Goldstein, M. L., Besser, B. P., & Fritzer, J. M. 2000, *JGR*, 105, 12675
- Usmanov, A. V., Goldstein, M. L., & Matthaeus, W. H. 2012, *ApJ*, 754, 40
- Usmanov, A. V., Goldstein, M. L., & Matthaeus, W. H. 2014, *ApJ*, 788, 43
- Usmanov, A. V., Matthaeus, W. H., Breech, B., & Goldstein, M. L. 2009, in *ASP Conf. Ser.*, 406, Numerical Modeling of Space Plasma Flows: ASTRONUM—2008, ed. N. V. Pogorelov et al. (San Francisco, CA: ASP), 160
- Usmanov, A. V., Matthaeus, W. H., Breech, B., & Goldstein, M. L. 2011, *ApJ*, 727, 84
- Vasyliunas, V. M., & Siscoe, G. L. 1976, *JGR*, 81, 1247
- Wang, C., & Richardson, J. D. 2001, *JGR*, 106, 29401
- Washimi, H., & Tanaka, T. 1996, *SSRv*, 78, 85
- Whang, Y. C. 1996, *ApJ*, 468, 947
- Whang, Y. C. 1998, *JGR*, 103, 17419
- Whang, Y. C. 2010a, *ApJ*, 713, 721
- Whang, Y. C. 2010b, *ApJ*, 710, 936
- Whang, Y. C., Burlaga, L. F., & Ness, N. F. 1995, *JGR*, 100, 17015
- Whang, Y. C., Burlaga, L. F., Wang, Y.-M., & Sheeley, N. R. 2003, *ApJ*, 589, 635
- Wiengarten, T., Fichtner, H., Kleimann, J., & Kissmann, R. 2015, *ApJ*, 805, 155
- Williams, L. L., Zank, G. P., & Matthaeus, W. H. 1995, *JGR*, 100, 17059
- Wu, C. S., & Davidson, R. C. 1972, *JGR*, 77, 5399
- Yokoi, N., Balarac, G., & Kitiashvili, I. N. 2010, in *Proc. of the Summer Program 2010* (Stanford, CA: Center for Turbulence Research, Stanford University), 493
- Yokoi, N. 2011, *JTurb*, 12, 1
- Yokoi, N., Rubinstein, R., Yoshizawa, A., & Hamba, F. 2008, *JTurb*, 9, 1
- Zank, G. P., Dosch, A., Hunana, P., et al. 2012, *ApJ*, 745, 35
- Zank, G. P., Pauls, H. L., Williams, L. L., & Hall, D. T. 1996, *JGR*, 101, 21639
- Zhou, Y., & Matthaeus, W. H. 1990, *JGR*, 95, 10291